

Chapter 1 Introduction

1.1. Photonic Crystals

While electronic device microminiaturization is close to reaching its maximum possible potential, photonic devices have unique properties that have yet to be exploited. The vision of miniaturized photonic devices will be realized only when we can sufficiently manipulate light on the sub-micrometer scale similar to what has been achieved for electrons in semiconductor devices. Photonic crystals have emerged as feasible solutions to answer this need for a wide range of devices including single photon sources, lasers, light emitting diodes (LEDs), detectors, filters, waveguides, and optical circuits.

The basic concept of photonic crystals was first proposed by E. Yablonovitch in 1987 [1]. In the article, it mention that the spontaneous emission can be forbidden if a periodic dielectric structure has an electromagnetic band gap which overlaps the electronic band edge. According to this concept, we could design periodic materials to control the optical properties of materials. Such as, prohibit or allow the propagation of light in certain directions at specified frequencies, and localize light in specified areas. Therefore, a crystal which was arranged in periodic and had ability to control the flow of light we called photonic crystals.

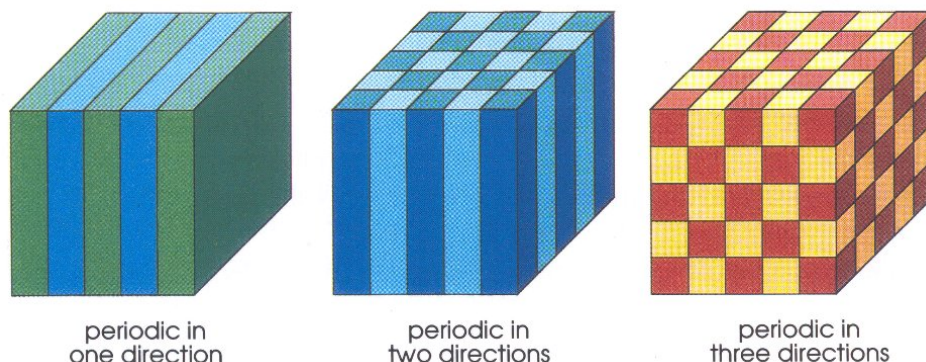


Figure 1.1 The schematic illustration of one-, two-, and three-dimensional photonic crystals. Different dielectric constants were represented in the different colors. (Adopted from reference [2])

These artificial structures are characterized by one-dimensional (1-D), two-dimensional (2-D), and three-dimensional (3-D) periodic arrangements of dielectric materials (Fig. 1.1) which lead to the formation of an energy band structure for electromagnetic waves propagating in them.

One of the most important features of photonic crystals is photonic band gap (PBG). As shown in Figure 1.1, the simplest photonic crystal consists of alternating layers of material with different dielectric constants. Bragg diffraction in these periodic arrangements results in light interference manifested photonic band gaps, where propagation of certain frequencies of electromagnetic radiation is inhibited. This one-dimensional photonic crystal, therefore, can act as a perfect mirror for light with a frequency within a sharply-defined gap. In the Figure 1.2, the reflectivity of this structure between the light wavelengths 1380nm to 1650nm is equal to 1. The concept had wide range application is distributed Bragg reflectors (DBRs).

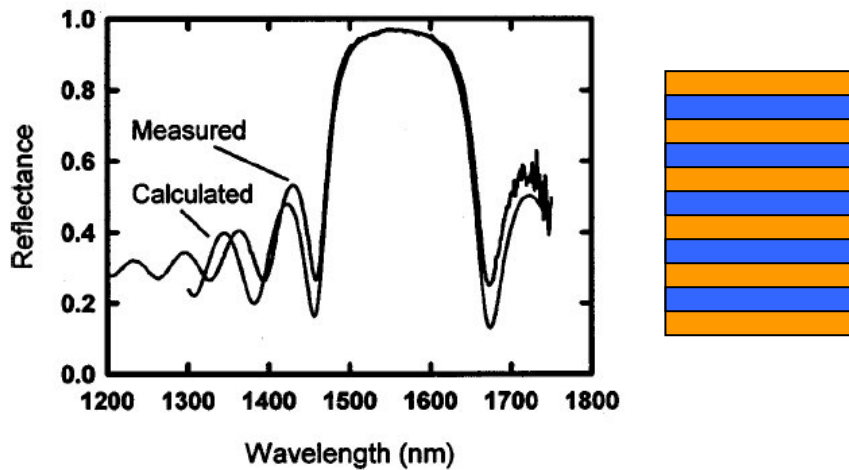


Figure 1.2 A typical reflectance spectra for the AlGaPSb/InP at 1550nm DBR (Adopted from reference [3]). The schematic at right side is a simple structure of DBR.

In order to study the bandstructure and the characteristic PBG of photonic crystals, we can easily realize from the theorem of solid state physics. In the typical electric material

theory, the motion of electronic wave in periodic atomic crystal obeys time-independent Schrodinger equation :

$$\left[-\frac{\hbar}{2m^*} \nabla^2 + V(r) \right] \psi(r) = E \psi(r) \quad (1.1)$$

where m^* is the effective mass of electron, $V(r)$ is the potential of periodic arrangement crystal, $\psi(r)$ is the function of electronic wave, the square of $\psi(r)$ denotes the existence probabilities of electrons in space, and E is eigen-value of electron energy. If the $\psi(r)$ term is equal to zero in some energy levels, electronic band gaps will exist in electronic band structure. Supposing the lattice potential is strong enough, the gap might extend to all possible directions, resulting in a complete band gap.

The optical analogy is photonic crystal, in which the periodic potential is due to a lattice of macroscopic dielectric media instead of atoms. If the dielectric constants of the materials in the crystal are different enough, and the absorption of light by the material is minimal, then scattering at the interfaces can produce many of the same phenomena for photons as the atomic potential does for electrons [2]. Deriving from the equation (1.1) and Maxwell's equations, we get a following master equation which expands on the behavior of photons moving in photonic crystals.

$$\nabla \times \left(\frac{1}{\varepsilon(r)} \nabla \times H(r) \right) = \left(\frac{\omega}{c} \right)^2 H(r) \quad (1.2)$$

where $\varepsilon(r)$ is the dielectric constant with periodic variation function in space. For a given frequency ω , we can solve the equation (1.2) and get the corresponding mode profile $H(r)$. Following this calculation, the corresponding eigen-values and eigen-vectors can be obtained. The wave vectors tell how the phase of the mode varies with position, and the band number increases with frequency. Consequently, a photonic band structure can be shown by calculation.

In Figure 1.3, there is a gap in frequency between the upper and lower branches of the lines, air band and dielectric band, respectively. The gap in specific frequency which has no mode and can exist in the crystal we called a photonic band gap.

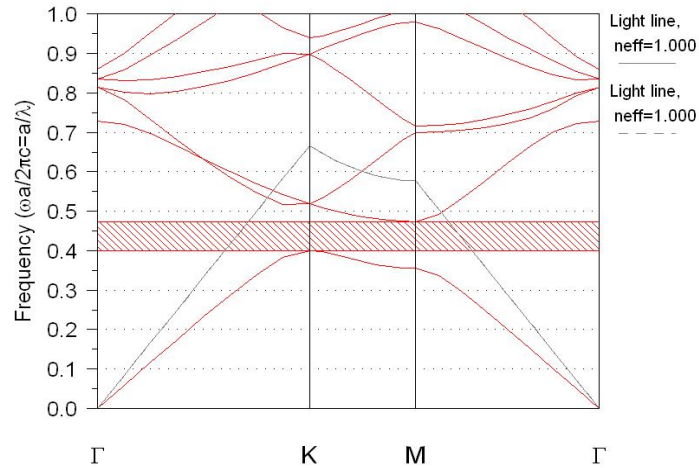


Figure 1.3 A typical TE mode 2-D photonic crystals band structure calculated by 2-D plane-wave expansion (PWE) method. The shadow region is the PBG of this 2-D photonic crystals with $r/a = 0.3$, $a = 500$ nm.

Furthermore, when we want to use the PBG effect, it is important to construct photonic crystals which the PBGs correspond to the wavelengths to be utilized. It is necessary to introduce artificial defects to manipulate photons inside the crystals. There are two common examples for study, including light localization at point defects (Fig. 1.4(a)) and propagation through line defects (Fig. 1.4(b)). The light in specific frequency localized or propagated in these defects will get ultra-low loss because of the PBG effect.

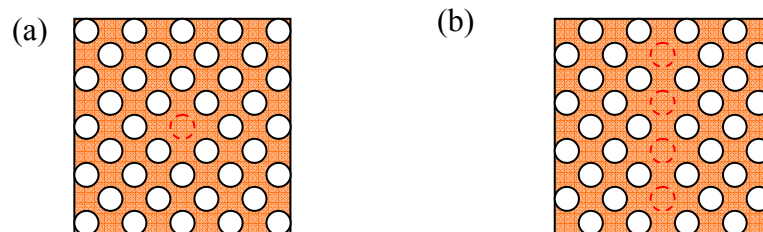


Figure 1.4 The illustrations show 2-D PCs with (a) a point defect by removing one air hole. (b) a line defect by removing one row of air holes.

1.2. Photonic Crystal Lasers

Introducing point and line defects in the periodic photonic lattices give rise to localized modes within the band gaps and hence allow us to confine and manipulate the flow of light in these structures. This behavior is analogous to that seen in crystalline semiconductors thereby making photonic crystals excellent candidates for PBG and defect engineering. In the past decade, therefore, photonic crystal structures with their parameters design have been the subject of intense research and development.

The recent notable contributions of PCs to improvement of the existing common semiconductor light sources, including replacement of the cleaved laser facets with PCs [4], enhancement of vertical extraction efficiency in LEDs [5], reduction of refractive index in vertical cavity surface-emitting lasers (VCSELs) to improve the optical lateral confinement [6], and so on. When integrated with submicrometer-scale light emitters and detectors, these components could eventually lead to the realization of functional ultra-small high-density photonic integrated circuits [7] and wavelength division multiplexing (WDM) system in communication systems application [8].

In this thesis, we will focus on one of the most significant application of 2-D photonic crystals as a platform for a variety of microcavity lasers. And discuss the PBG engineering of a semiconductor laser which leads to achieve the property of high quality factor, small mode volume, and ultra-low threshold.

Typically, we can separate 2-D photonic crystal lasers into two different geometry, square lattice [9, 10] and triangular lattice [11, 12], according to lattice constant of photonic crystal. In the same r/a ratio, a photonic crystal laser with triangular lattice constant is much

easily demonstrated than a square one owing to the broader PBG (Fig. 1.5). However, the square lattice photonic crystal lasers could have smaller mode volume because of its lowest order whisper gallery mode. In recent years, therefore, there are some different design methods for photonic crystal lattice, in order to achieve further low-threshold and smaller mode volume. And we will mention another geometric design in the next section.

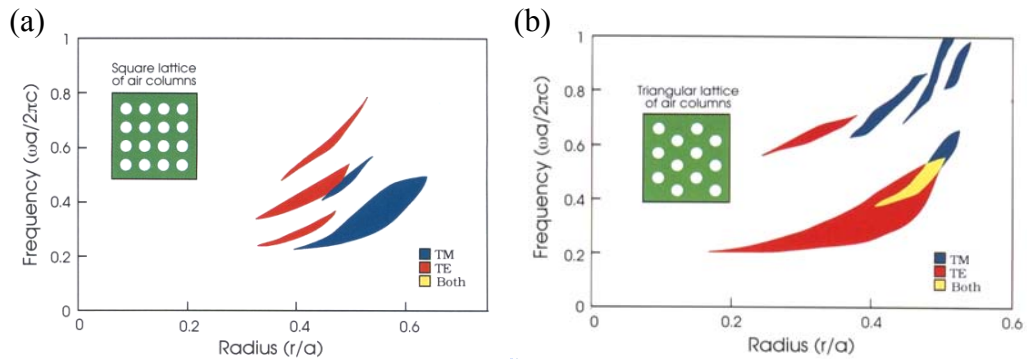


Figure 1.5 Gap map for a (a) square (b) triangular lattice of air columns with dielectric medium, $\epsilon = 11.4$. PBGs in a triangular lattice are usually broader than a square one, in the same r/a ratio. The yellow region in (b) is called a complete band gap which included the photonic band gaps with TM mode and TE mode. (Adopted from reference [2])

Two-dimensional photonic crystals with a triangular lattice of air-holes in membrane structure [13, 14] have become most popular systems used to study photonic crystal microcavity effects. A microcavity laser with a wide range of tailored modes excitable by the active layer within the cavity can be created by removing several selected air-holes lattice, or modifying the parameters of the inner holes near cavity region [14]. These structures have rather capable of confining light within microcavities with expressive high Q factors as a result of quasi-3D light confinement. As the Figure 1.6 shown, quasi-3D light confined with the in-plane confinement provided by the PBG and the vertical confinement by total internal reflection (TIR) provided by the cladding.

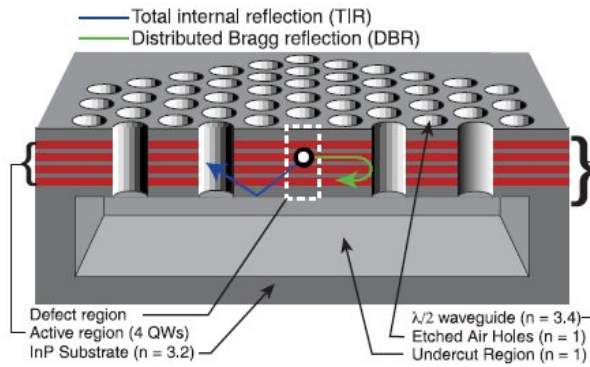


Figure 1.6 A scheme of cross section of the photonic crystal microcavity. The combination of distributed Bragg reflection from 2-D photonic crystal and TIR from the air cladding constructed a quasi-3D light confinement mode. (Adopted from reference [13])



1.3. Quasi-Periodic Photonic Crystal Lasers

On the previous sections, we propose that the anisotropy of a photonic band gap is dependent on the periodicity of the photonic crystal lattice. Their essential feature is the formation of Bloch states as a result of the periodic perturbation from the lattice with translational symmetry. In 1998, however, Chan *et al.* calculated the density of state in a quasi-periodic photonic crystal [15] instead of in the periodic one, and also found the complete photonic band gaps as well as triangular lattice photonic crystal.

Quasi-Periodic photonic crystals have neither true periodicity in real space nor translational symmetry. As we called, it has a quasi-periodicity that exhibits long-range order and rotational symmetry. In general, a periodic photonic crystal is represented the rotational symmetry order which less than 6-fold, such as triangular lattice photonic crystals. Any other order of rotational symmetry, 8-, 10-, 12-, 16-fold, etc. is possible in quasi-periodic photonic crystals. Recently, quasi-periodic photonic crystals are being studied [15-18] because of the larger degrees of freedom for modifying optical properties than in photonic crystals.

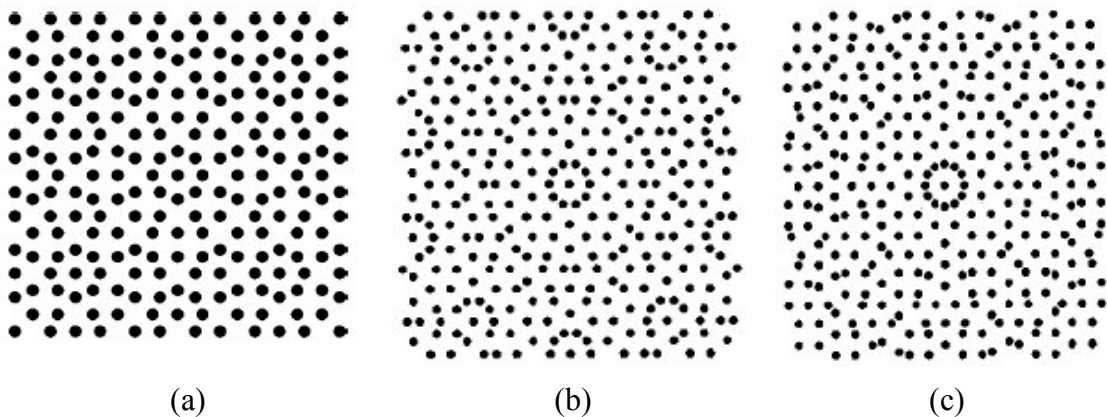


Figure 1.7 Schematic figures showing the (a) octagonal (b) decagonal (c) dodecagonal quasi-periodic photonic crystal patterns. (Adopted from reference [19, 20])

As the order of the rotational symmetry increase, the Brillouin zone becomes more circular, resulting in a complete band gap [16]. In order to achieve higher order of symmetry, certainly, the more complex geometries of quasi-periodic photonic crystals were being designed, as shown in Figure 1.7.

Up to date, few experimental efforts dealing with localized states in the quasi-periodic photonic crystals structure have been reported, such as that T. Baba. *et al.* have recently reported a whispering gallery mode (WGM) laser based on a quasi-periodic photonic crystals. So did the Y. H. Lee *et al.* [18], they reported the localized modes in a dodecagonal quasi-periodic photonic crystals single cavity laser. And modify the inner-most holes which are concentrated strongly on the dielectric region on purpose to achieve high quality factor.

The WGMs was significantly discussed from the resonant modes in microdisk and microgear lasers. For the microgear satisfying the condition that the grating number is equal to the number of WGM standing wave $2M$, the different phase non-lasing mode is completely suppressed by the enhancement of the field mismatch. In the opposite, for the inphase lasing mode, the lasing phenomenon is obtained by the strongly confined single mode (Fig. 1.8).

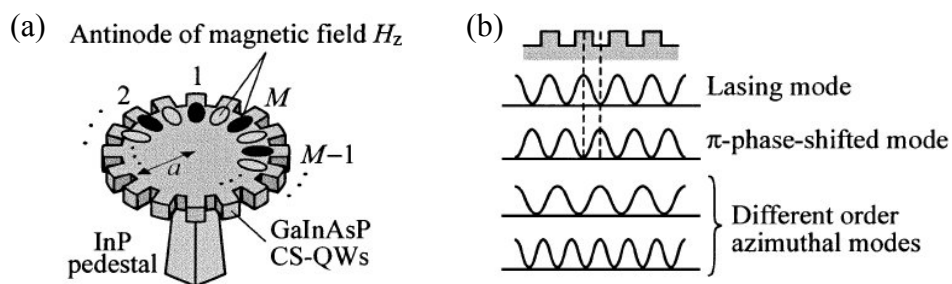


Figure 1.8 Schematics of a microgear laser and resonant modes. (a) The H_z standing wave of WGM matched with the grating number in this microgear laser. (b) The possible resonance modes of $|H_z|^2$. (Adopted from reference [17])

Because of the shape of quasi-periodic photonic crystals is approximate to the microgear lasers, we can also find the WGMs which sustained by one-dimensional TIR and two-dimensional PBG effect. A fusion with quasi-periodic photonic crystals and microgear lasers was demonstrated by T. Baba *et al.* in 2003. The fusion with quasi-periodic photonic crystals solved a problem of minimize restriction of cavity size in microgear laser [17].

Consequently, we consider the WGMs will be of potential use for quantum optics applications in addition to ultra-low threshold light source because the characteristic of the high concentration of the electromagnetic field energy on the dielectric region, the large separation from the other modes, and the high Purcell factor. In my thesis, we will focus on the study of quasi-periodic photonic crystals and its resonance modes.



1.4. An Overview of This Thesis

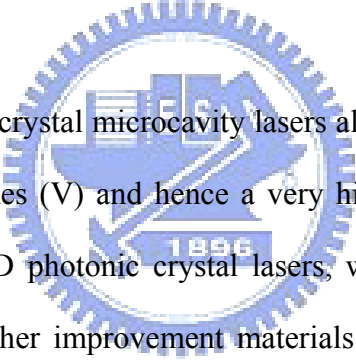
Photonic crystals have exhibited the best potential for achieving the final destination of microminiaturized photonic chips. In order to achieve this goal, more and more groups invest in 2-D or 3-D photonic crystals research. In this thesis, we will describe the current efforts of our group in photonic crystal microcavities.

The following series of chapters were included the basic theory of our design, simulation results, setup and procedures of fabrication, photoluminescence (PL) measurement results and analysis. The basic theory of QPC lasers and its simulation were introduced in the former chapter 2 and the structure design of devices in the latter. Fabrication procedure to membrane and bonding structure were demonstrated in chapter 3 and 4, respectively. And the problems in photonic crystal lasers fabrication were also discussed in detail in those chapters. In chapter 5, the basic lasing characteristics of 2-D photonic crystal lasers were measured by NIR micro-PL system. Besides, the measurement results were further compared and analyzed. A brief conclusion of my research in the past two years was presented in the last chapter.

Chapter 2 Device Structures

2.1. Introduction

The research of photonic crystals in the past decade was advancing at an astonishing step that proceeding from the concept of 1-D photonic crystals of DBR into 2-D photonic crystals and further to 3-D structures. In ideally, although, a 3-D photonic crystal with a defect microcavity formed by a missing period in the lattice would provide the best confinement for a light emitter placed inside the cavity, due to the PBG confinement in all spatial dimensions. While there are interesting results on 3-D photonic crystals in different material systems, it is practically difficult to fabricate cavities with sufficiently high Q in semiconductor based 3-D photonic crystals.



Two-dimensional photonic crystal microcavity lasers already can provide both high Q as well as ultra-small mode volumes (V) and hence a very high Q/V ratio. On the purpose to achieve the same quality as 3-D photonic crystal lasers, we replaced the vertical cladding layer by air, oxide, DBR, or other improvement materials. These structures that we called quasi-3-D photonic crystal lasers also provide light confinement from the horizontal two-dimensional PBG confinement and the vertical one-dimensional TIR confinement. In this chapter, we will introduce some different structures in study.

Necessarily, we used several numerical analysis methods to verify our designs and measurement results. The band diagrams of periodic symmetry photonic crystals and the resonance modes in microcavity were calculated by three-dimensional plane-wave expansion (PWE) method and two-dimensional finite-difference time-domain (FDTD) method, respectively. The simple theory of simulation will be discussed and its preliminary simulated results in the latter of this chapter.

2.2. Devices Structures

We have a common goal to fabricate the devices at communication wavelength. Then, the active epitaxial layer of our devices had a PL spectral bandwidth from 1480 to 1580 nm and centered at 1550nm (Fig. 2.1(b)). As shown in Figure 2.1(a), the epitaxial structure consists of four 10 nm 0.85% compressively strained InGaAsP quantum wells (QWs) which are separated by 20 nm unstrained InGaAsP barriers.

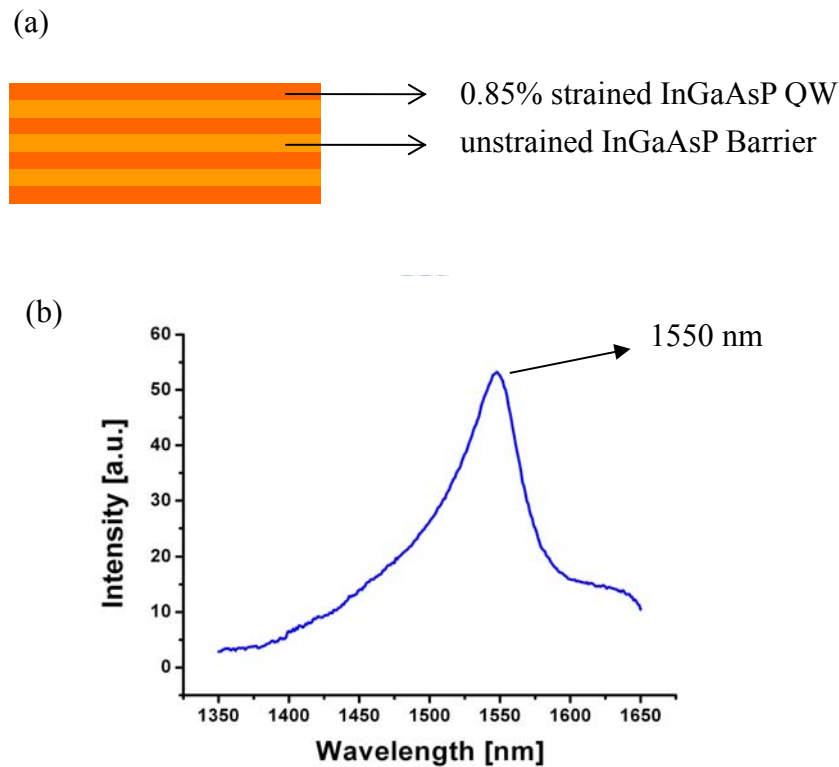


Figure 2.1 (a) Schematics of our designed epitaxial QWs structure. (b) A typical PL spectrum of our MQWs. It is centered at 1550 nm with 200nm span.

There are two different types of structure in our two-dimensional photonic crystal lasers. One is symmetric structure, and the other is asymmetric structure. In a symmetric structure, we fabricated the QWs slab as a thin dielectric membrane surrounded by upper and lower air cladding. Inversely, the asymmetric QWs slab was surrounded by different material clad layer. Those fabrication procedures in detail will be introduced in chapter 3 and chapter 4.

2.2.1. Membrane Structures

Membrane slab was one of the most popular structures in research, such as J. D. O'Brien, T. Baba, S. Noda. et al. were reported their important achievement by using membrane structure . A 2-D photonic crystal slab, as shown in Figure 2.2, with promising, owing to strong optical confinement for both in-plane and vertical directions. The PBG effect is used for light confinement as perfect mirrors in the in-plane direction, and TIR effect at the interface between the slab and the air clad in the vertical direction. Because of the fulfillment strong light confinement condition in microcavity, high Q/V ratio can easily achieved by this structure design.

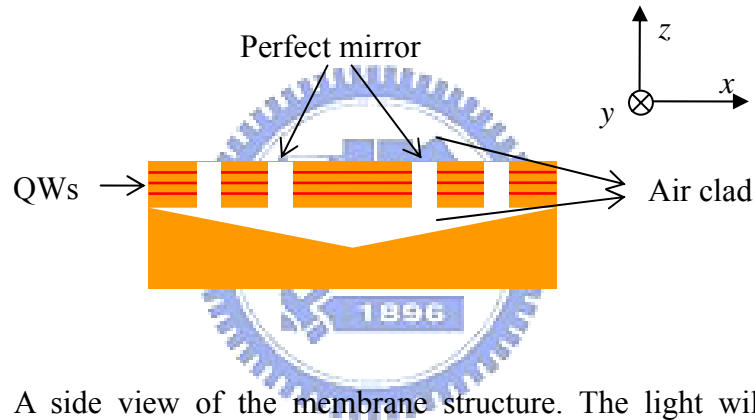


Figure 2.2 A side view of the membrane structure. The light will be confined in membrane structure by perfect mirrors for the x direction, and by the air clad based on TIR for the z direction.

2.2.2. Wafer Bonding Structures

In the asymmetry structures, a photonic crystal QWs slab is the same as previous designed but the lower air cladding layer is replaced by a sapphire or a DBR substrate in our design. For asymmetry structures, they can improve the thermal effect which is produced from optical pumping on the membrane structure microcavity. The thermal effect seriously caused high threshold value and red shift in wavelength of a photonic crystal laser [21]. Although asymmetry structures could solve the thermal effect problem,

light in the dielectric region would get larger optical loss comparing to the membrane structure.

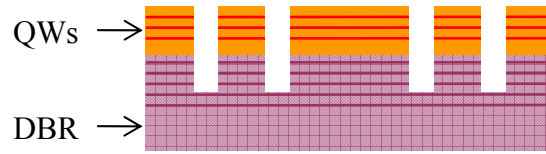


Figure 2.3 The illustrations of 2-D photonic crystal asymmetric structure bonding with DBR substrate in side view.

As Figure 2.3 shown, we designed a structure which is the QWs slab bonding to a DBR($\text{GaAs}/\text{Al}_{0.9}\text{Ga}_{0.1}\text{As}$) substrate. The reason why we chose DBR is owing to the good thermal conductivity. In table 2.1, we can know about the thermal conductivity and refractive index with different material. Obviously, the thermal conductivity of sapphire is about 4000 times larger than that of air. It seems to more other materials can be used in table 2.1 such like silicon and copper. But these materials caused another problem that the vertical optical confinement will become weaker than DBR if choose a smaller refractive index contrast to InP. Then, it will cause to lower Q factor of the lasing mode because of the larger optical loss in vertical direction. Consequently, we weighted the advantages in both conditions and chose the DBR to be used for bonding with QWs.

Table 2.1 The thermal conductivities and refractive indices with different materials.

Material	Air	Sapphire	Si	Cu	GaAs	$\text{Al}_{0.9}\text{Ga}_{0.1}\text{As}$	InP
Thermal Conductivity ($\text{W}/\text{cm}\cdot^{\circ}\text{C}$)	0.00016	0.35	1.3	3.937	0.55	0.65	0.68
Refractive Index	1	1.77	3.42	2.43	3.3	2.9	3.1

The application of DBR structure was widely used in VCSEL. And following the concept in VCSEL, we design a QWs slab bonding with DBR substrate as shown in Figure 2.3. Our DBR structure is composed of 22 pairs of GaAs/Al_{0.9}Ga_{0.1}As layer and the reflectivity in the wavelength from 1450 to 1600 nm is up to 99.5% (Fig. 2.4). That DBR substrate has not only the advantage in thermal conductivity but a better vertical optical reflectance than air in specific wavelength. As we mention previously, the DBR substrate can be seemed to a 1-D photonic crystal that confined the light in vertical direction. In theory, therefore, the asymmetry structure of DBR could have a lower threshold and higher Q factor due to the better thermal conductivity and lower optical loss, respectively.

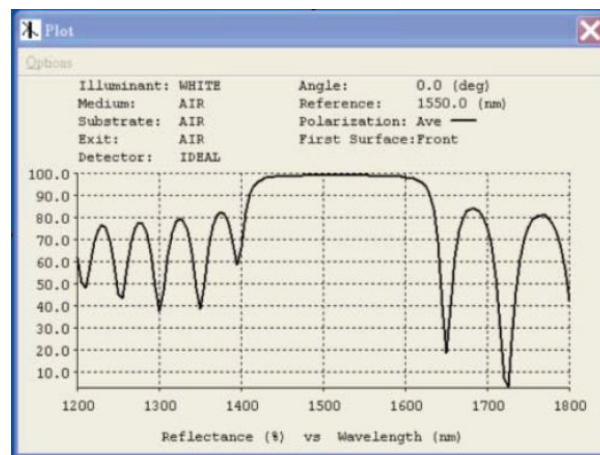


Figure 2.4 The calculated reflectivity of DBR which can be up to 99.5% in the wavelength from 1450 to 1600 nm.

2.3. Quasi-Periodic Photonic Crystal Lasers

We had introduced the designed structures that we used in our research. And the following section will focus on the design of the photonic crystals pattern. The motivation for using a QPC is to maintain the periodic scattering of light while reducing the orientational order of the system so that it is more isotropic. In theory, a higher order of QPC laser would eliminate wave-guiding modes coincident with the PBG and a smaller value of threshold should be determined.

2.3.1. Basic Theory of Quasi-Periodic Photonic Crystal Lasers

On the basis of previous theoretical studies, it is evident that the anisotropy of a PBG is dependent on the symmetric photonic crystal lattice. But in an asymmetric photonic crystal lattice, how could the photon affect that QPCs have the same PBG phenomenon with symmetric PCs. Clues to the scattering properties of the QPC may be found in the reciprocal lattice space (Fig. 2.5). While the edges of Figure 2.5 extend to the basic reciprocal vector ($2\pi/a$) (Fig. 2.6), a dodecahedral Brillouin zone be indicated. In the triangular or square lattice of the same near lattice distance would have a sparse reciprocal lattice. The quasi-periodic photonic crystals, however, has more order symmetries that average out the anisotropy, but provide additional resonant scattering conditions.

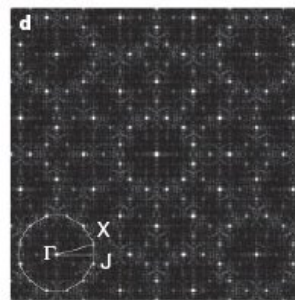


Figure 2.5 A dodecagonal QPCs in reciprocal lattice space. (Adopted from reference [16])

Moreover, there is another important characteristic of QPCs. As we mentioned in chapter 1.3, a well-confined whispering gallery mode should be enhanced by a modified QPC microcavity laser. The basic theory of WGM was significantly discussed from the resonance mode in microgear laser. In Figure 1.8(b), the microgear laser has a grating at the disk edge with a period equal to the half wavelength of the WGM. The 2-D FDTD analysis with the effective index approximation explained the strong optical confinement and the single-mode operation as follows.

If assume that only TE-polarized modes are allowed due to the electron transition between the conduction band and the valence band in compressively-strained quantum-wells. Then, the normal component of the magnetic field H_z and the radial component of the electric field E_r generate the WGM energy, while H_z and the azimuthal component of the electric field E_θ generate the radiation power to outside of the cavity. E_r is discontinuous at the disk boundary, so it penetrates into air more deeply than H_z . To compensate for this difference, E_θ is excited, and this results in radiation loss. In microgear lasers, however, the penetration depths of E_r and H_z are equalized by the grating. Therefore, the generation of E_θ is suppressed, and the Q factor is increased. Additionally, E_θ of the π -phase-shifted mode is more excited and its Q factor is reduced. Thus, this mode is suppressed and the stable single mode is realized [17].

2.3.2. 12-fold Quasi-Periodic Photonic Crystal Lasers

As the order of the symmetry increases, the inner-most points in Brillouin zone become more circular (Fig. 2.6). The higher order of rotational symmetry, 8-, 10-, 12-,

16-fold, etc. is possible in quasi-periodic photonic crystals. In our group, the octagonal, dodecagonal quasi-periodic photonic crystals and circular photonic crystals were demonstrated. In my work, I was focus on the characteristic of dodecagonal QPCs. There are twelve white spots around the origin of the reciprocal space which is transfer from the unit cell by Fourier transform (Fig 2.6).

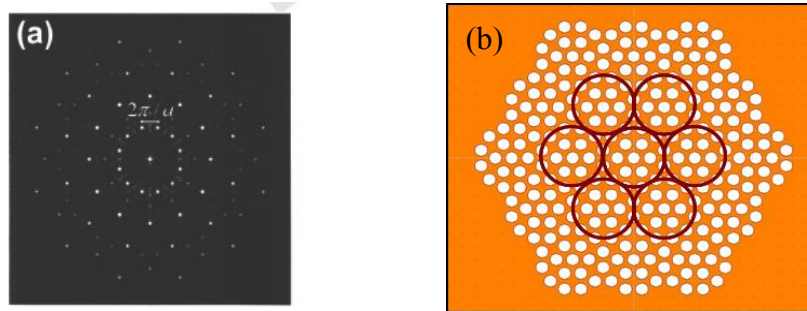


Figure 2.6 (a) The scheme shows a dodecagonal structure in basic reciprocal space.(Adopted from reference [18]) (b) The circle represents a unit cell of a dodecagonal QPCs.

In dodecagonal QPCs, three different missing air-holes microcavity lasers would be discussed. As the shown in Figure 2.7, it illustrated the dodecagonal QPCs with 1, 7, and 19 missing air holes. The lager microcavity laser has more resonance modes in the dielectric region than the smaller one as the same phenomenon in basic PC lasers. Therefore, in measurement, the 12-fold QPC laser with 1 missing air-hole is more difficult to lase than others.

Besides, a larger microcavity laser has bigger area of dielectric region where leads the photons getting more photon lifetime than smaller one. In theory, the photon which has more photon lifetime can enhance a higher Q factor. But in 12-fold D2 QPC laser, a higher Q factor will be obtained from the WGM with azimuthal number six. In D3 QPC laser, the inner-most air-holes in microcavity dose not similar to the microgear cavity as

D2 QPC laser. Therefore, a better Q factor and the smaller threshold would be obtained from D2 QPC laser.

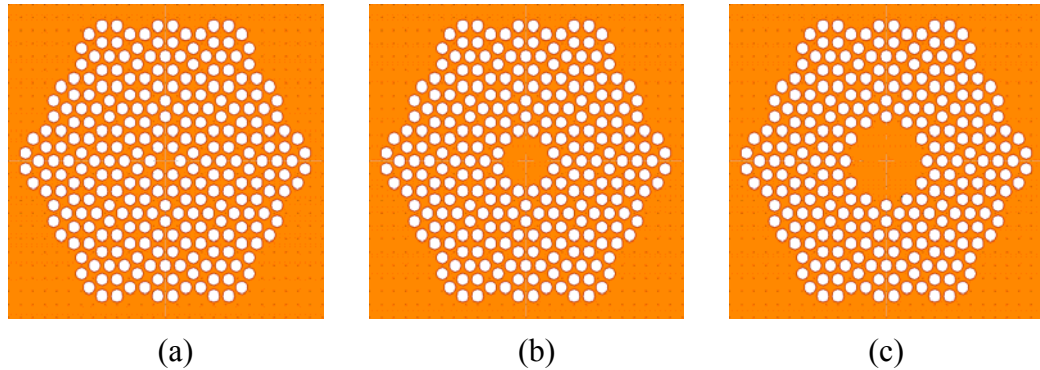


Figure 2.7 The illustration of dodecagonal QPCs with (a) 1 (b) 7 (c) 19 air holes. D1 represent the meaning of 1 missing air hole and D2 represent 7, D3 represent 19 missing air holes, etc.

High quality factor whispering gallery mode can be sustained in QPC micro-cavity with proper modification. In order to obtain the well-confined WGM, the constructive interference condition has to be satisfied at the cavity boundary and the standing wave should be formed in the nearest air holes of a microgear like cavity. Figure 2.8 shows the design of the 12-fold modified QPC microcavity laser. The well-confined WGM profile in magnetic field with azimuthal number six of the modified microcavity should be obtained. And the number of lobes would match with the number of gears.

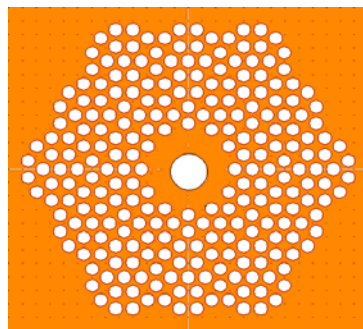


Figure 2.8 The scheme illustrate the design of the 12-fold modified QPC microcavity laser.

2.3.3. Finite-Different Time-Domain Method

To solve the differential form of Maxwell's equations, we can replace the differential form with differencing form, and expand the differencing form to obtain the basic Finite-Difference Time-Domain (FDTD) equation. Because the time-domain technique can cover a wide frequency range with single simulation run, FDTD method is the one of the most popular method to simulate the electromagnetic wave in the photonic crystal.

As simulating by FDTD method, Maxwell's curl equations are given in the following:

$$\begin{aligned}\nabla \times \bar{E} &= -\frac{\partial \bar{B}}{\partial t} - \bar{J}_m \\ \nabla \times \bar{H} &= \frac{\partial \bar{D}}{\partial t} + \bar{J}_e\end{aligned}\quad (2.1)$$

where \bar{J}_e and \bar{J}_m denote electric current source and magnetic current source. Then, we substitute the relation of them into equation (2.1). We can obtain:

$$\begin{aligned}\frac{\partial \bar{E}}{\partial t} &= \frac{1}{\varepsilon} \nabla \times \bar{H} - \frac{\sigma}{\varepsilon} \bar{E} \\ \frac{\partial \bar{H}}{\partial t} &= -\frac{1}{\mu} \nabla \times \bar{E} - \frac{\rho'}{\mu} \bar{H}\end{aligned}\quad (2.2)$$

where ε is the electrical permittivity, μ is the magnetic permeability, σ is the electrical conductivity, and ρ' is an equivalent magnetic resistivity. The magnetic resistivity term is provided to yield symmetric curl equations. By the Maxwell's divergence equation $\nabla \cdot \bar{B} = 0$, \bar{J}_m is absent. Therefore, The magnetic resistivity term is absent. Because of small variation of magnetic permeability in materials, We assume that the magnetic permeability in materials is equal to that in free space, μ_0 . And the material is

assumed to be lossless, which implies that σ is equal to zero. In a rectangular coordinate system, equation (2.2) is equal to the following system of scalar equations :

$$\frac{\partial H_x}{\partial t} = \frac{1}{\mu_0} \left(\frac{\partial E_y}{\partial z} - \frac{\partial E_z}{\partial y} \right) \quad (2.3)$$

$$\frac{\partial H_y}{\partial t} = \frac{1}{\mu_0} \left(\frac{\partial E_z}{\partial x} - \frac{\partial E_x}{\partial z} \right) \quad (2.4)$$

$$\frac{\partial H_z}{\partial t} = \frac{1}{\mu_0} \left(\frac{\partial E_x}{\partial y} - \frac{\partial E_y}{\partial x} \right) \quad (2.5)$$

$$\frac{\partial E_x}{\partial t} = \frac{1}{\varepsilon} \left(\frac{\partial H_z}{\partial y} - \frac{\partial H_y}{\partial z} \right) \quad (2.6)$$

$$\frac{\partial E_y}{\partial t} = \frac{1}{\varepsilon} \left(\frac{\partial H_x}{\partial z} - \frac{\partial H_z}{\partial x} \right) \quad (2.7)$$

$$\frac{\partial E_z}{\partial t} = \frac{1}{\varepsilon} \left(\frac{\partial H_y}{\partial x} - \frac{\partial H_x}{\partial y} \right) \quad (2.8)$$

The six partial differential equations are the basic the FDTD equations. To do numerical calculation, we shall transform differential equations above into differencing equations. We denote a space point in a rectangular lattice as :

$$(i, j, k) = (i_{\Delta x}, j_{\Delta y}, k_{\Delta z}) \quad (2.9)$$

and for any function of space and time we put :

$$F^n(i, j, k) = F(i_{\Delta x}, j_{\Delta y}, k_{\Delta z}, n_{\Delta t}) \quad (2.10)$$

where Δx , Δy , and Δz are the lattice space increments in x, y, z coordinate direction, Δt is the time increment, and i, j, k , and n are integers. By using the centered finite-difference approximation for the spacial and temporal differential equations, we can obtain :

$$\begin{aligned}
\frac{\partial F^n(i, j, k)}{\partial x} &= \frac{F^n(i + \frac{1}{2}, j, k) - F^n(i - \frac{1}{2}, j, k)}{\Delta x} \\
\frac{\partial F^n(i, j, k)}{\partial y} &= \frac{F^n(i, j + \frac{1}{2}, k) - F^n(i, j - \frac{1}{2}, k)}{\Delta y} \\
\frac{\partial F^n(i, j, k)}{\partial z} &= \frac{F^n(i, j, k + \frac{1}{2}) - F^n(i, j, k - \frac{1}{2})}{\Delta z} \\
\frac{\partial F^n(i, j, k)}{\partial t} &= \frac{F^{n+\frac{1}{2}}(i, j, k) - F^{n-\frac{1}{2}}(i, j, k)}{\Delta t}
\end{aligned} \tag{2.11}$$

To substitute equation (2.11) into equation (2.3 – 2.8), Yee put the components of

\bar{E} and \bar{H} at an unit cell of rectangular lattice And Yee evaluated \bar{E} and \bar{H} at alternate half time step as shown in Figure 2.9 :

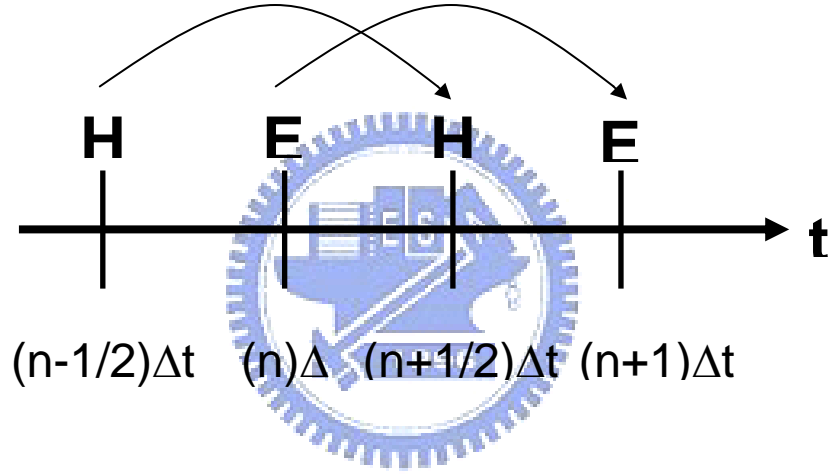


Figure 2.9 Temporal division of \bar{E} and \bar{H} components.

Then, we substitute equation (2.11) into equation (2.5) and equation (2.8) to obtain

\bar{E} and \bar{H} components in the z-direction, we have :

$$\begin{aligned}
H_z^{n+\frac{1}{2}}(i + \frac{1}{2}, j + \frac{1}{2}, k) &= H_z^{n-\frac{1}{2}}(i + \frac{1}{2}, j + \frac{1}{2}, k) + \frac{\Delta t}{\mu_0} \cdot \left\{ \frac{1}{\Delta y} [E_x^n(i + \frac{1}{2}, j + 1, k) - E_x^n(i + \frac{1}{2}, j, k)] \right. \\
&\quad \left. - \frac{1}{\Delta x} [E_y^n(i + 1, j + \frac{1}{2}, k) - E_y^n(i, j + \frac{1}{2}, k)] \right\}
\end{aligned} \tag{2.12}$$

$$\begin{aligned}
E_z^{n+1}(i, j, k) &= E_z^n(i, j, k + \frac{1}{2}) + \frac{\Delta t}{\varepsilon(i, j, k + \frac{1}{2})} \cdot \left\{ \frac{1}{\Delta x} [H_y^{n+\frac{1}{2}}(i + \frac{1}{2}, j, k + \frac{1}{2}) - H_y^{n+\frac{1}{2}}(i - \frac{1}{2}, j, k + \frac{1}{2})] \right. \\
&\quad \left. - \frac{1}{\Delta y} [H_x^{n+\frac{1}{2}}(i, j + \frac{1}{2}, k + \frac{1}{2}) - H_x^{n+\frac{1}{2}}(i, j - \frac{1}{2}, k + \frac{1}{2})] \right\}
\end{aligned} \tag{2.13}$$

The equations corresponding to equation (2.3), (2.4), (2.6), (2.7) can be similarly constructed. By the system of finite-difference equations, the new value of the \bar{E} and \bar{H} component at any lattice point depends only on its previous value and on the previous values of the \bar{E} and \bar{H} component at adjacent points.

There are many electromagnetic calculation for infinite dielectric space, but the practical simulation can calculate infinite dielectric space problem. Therefore, the calculated dielectric space has to be appropriately downscaled. Then, we make an artificial boundary and the electromagnetic field will vanish the artificial boundary.

As the electromagnetic wave propagates in homogeneous dielectric, the propagating velocity in the x, y, z direction is the same. But the propagating velocity in the diagonal direction is faster than that in the x, y, z direction. Therefore, the simulating wave will cause distortion as the propagating time increase. In order to reduce the space error between the x, y, z direction and the diagonal direction, the space grid size must be chosen such that an increment of the electromagnetic field does not change significantly. And the time grid size is also chosen for the stability. For constant ε and μ , computational stability implies :

$$\Delta t \leq \frac{1}{c \sqrt{\left(\frac{1}{\Delta x}\right)^2 + \left(\frac{1}{\Delta y}\right)^2 + \left(\frac{1}{\Delta z}\right)^2}} \quad (2.14)$$

This requirement puts a restriction on Δt for our chosen Δx , Δy , and Δz .

2.3.4. Band Structure and Mode Analysis

According to the QPC has no translational symmetry to calculate the PBG in 2D PWE method. The transmission spectra for a supercell of 12-fold QPCs were obtained by 2D FDTD method. Figure 2.10 shows the transmission spectra calculated from $r/a = 0.36$ to 0.42 in two different incident angles degree a and degree b. The transmission is strongly suppressed in frequency ranges PBG both A and B. Therefore, these frequency ranges can be thought as PBGs of the 12-fold QPC laser. For calculating a larger range of r/a ratio with transmission spectra, the PBG of the 12-fold QPC laser can be illustrated.

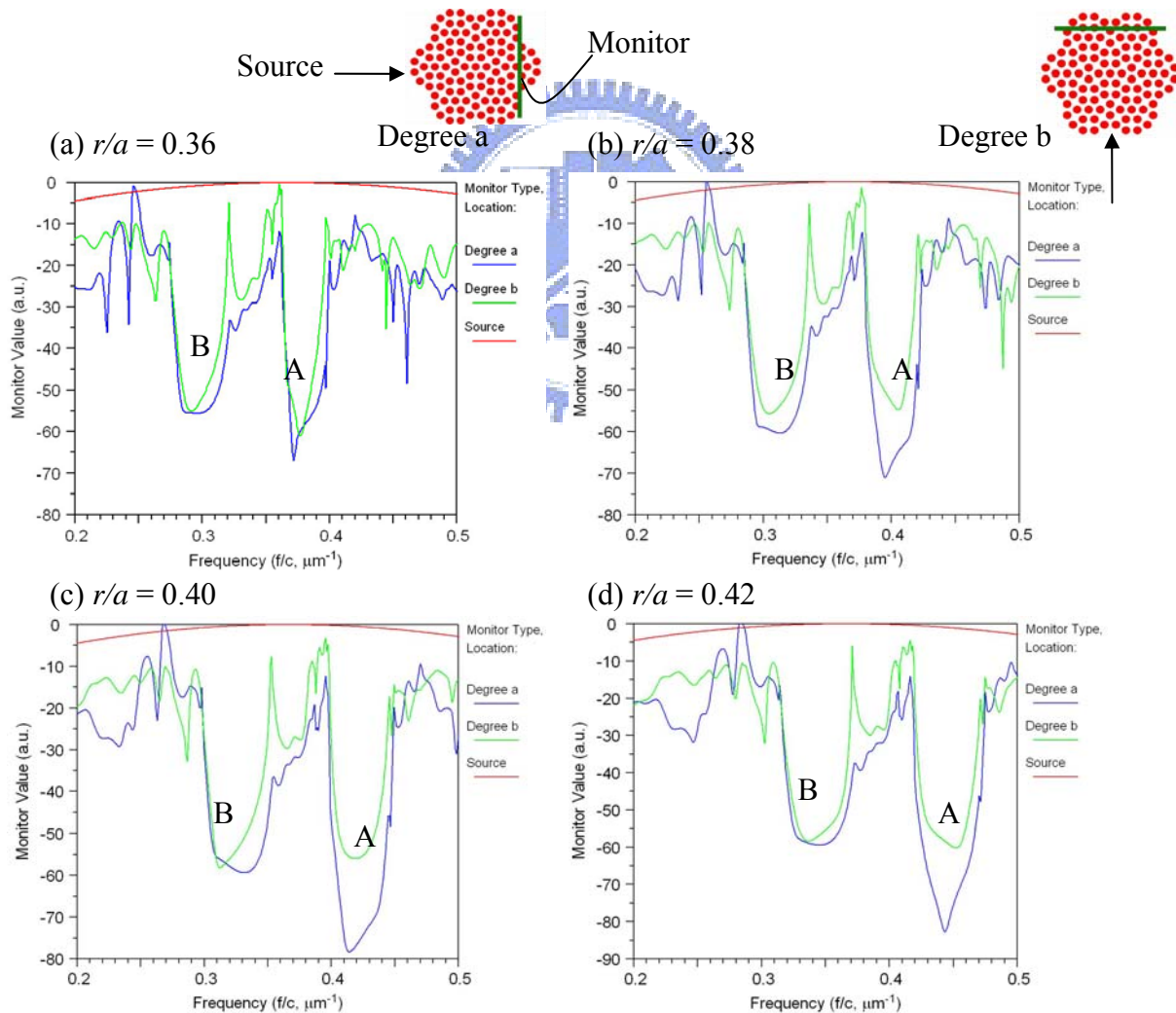


Figure 2.10 Transmission spectra of 12-fold QPCs from $r/a = 0.36$ to 0.42 . The inserts show the simulation structure and illustrates the position of source and detector.

In the Figure 2.11, it shows the normalized frequency a/λ of lasing modes with the normalized hole radius r/a . The distribution of dashed lines show calculated results of the PBG region which indicated the photonic gap of frequency. The solid lines show the simulated resonance modes in 12-fold D2 QPC laser with different r/a ratio. Three modes observed for different lattice constants a are WGMs having different azimuthal orders, as understood from calculated field distributions. As we discussed above, the lowest threshold should be the WGM mode with azimuthal number six, whose number of standing wave matches with the number of inner-most air-holes.

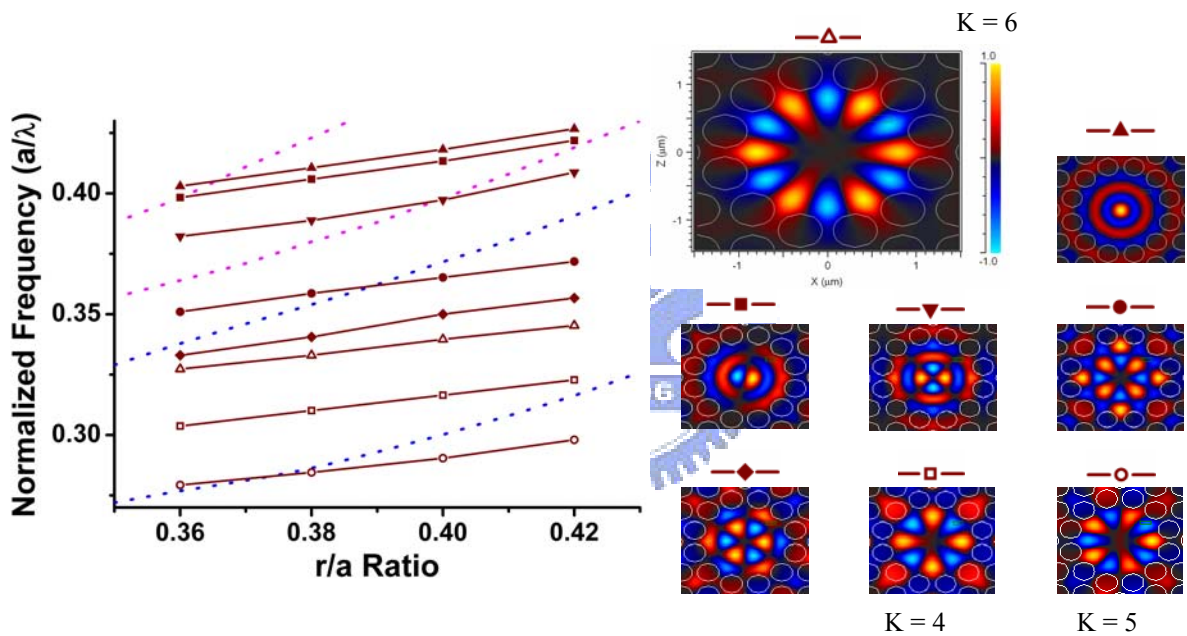


Figure 2.11 The illustration shows the normalized frequency of calculated lasing modes with the different normalized hole radius. The mode profiles on the right correspond to their symbols in the scheme on the left. The hollow symbols with solid lines show the different kinds of WGMs.

2.4. Conclusion

In this chapter, the basic theory of structure design was introduced as first. And then, the theory of photonic crystal and quasi-periodic photonic crystal (PC/QPC) lasers with different microcavities were presented. Finally, the band diagrams and the photonic band gap of two-dimensional quasi-periodic photonic crystals with different lattice parameters including lattice constants and radius of air holes are calculated by three-dimensional plane-wave expansion method. All of the resonance modes of 12-fold D2 QPC microcavity are calculated by two-dimensional finite-difference time-domain method.



Chapter 3 Fabrication of Membrane Structure Photonic Crystal Lasers

3.1. Introduction

The basic design principles and simulated results in membrane structure have been introduced in chapter 2. In this chapter, the fabrication procedures of membrane structure lasers in detail and the problems in process will be presented. Certainly, the modified fabrication processes will also be introduced in each section.

3.2. Fabrication of Two-Dimensional Photonic Crystal Lasers

The epitaxial structure of InGaAsP strained/unstrained QWs structure has been introduced in chapter 2.2. A completely structure for membrane fabrication is shown in Figure 3.1. The epitaxial structure consists of four 10 nm 0.85% compressively strained InGaAsP quantum wells which are separated by three 20 nm unstrained InGaAsP barrier layers. It has been confirmed that the PL spectrum of the QWs (Fig. 2.1(b)) is centered at 1550 nm with 200 nm span. The QWs was grown on InP substrate by metalorganic chemical vapor deposition (MOCVD) and then a 60 nm InP cap layer was deposited on it for protecting the QWs during a series of dry etching processes.

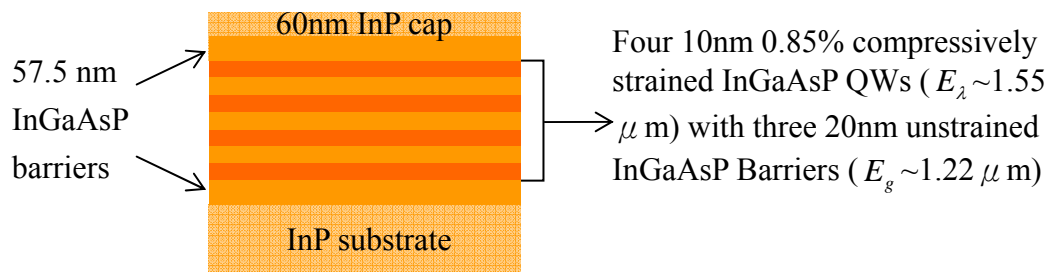
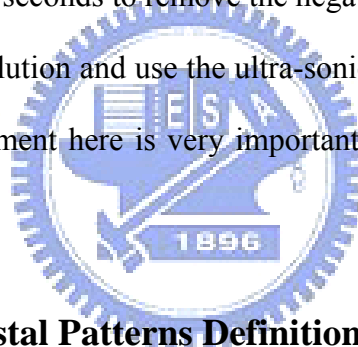


Figure 3.1 A illustration of epitaxial structure of InGaAsP QWs for membrane PC lasers. The thickness of active region is about 220 nm.

3.2.1. Dielectric Deposition

After the epitaxial growth, we deposited a 140 nm thick Si_3N_4 layer as an etching hard mask by SAMCO PD-220 plasma enhanced chemical vapor deposition (PECVD) process. The thickness of Si_3N_4 was decided depend on the selective dry etching ratio in ICP/RIE pattern transfer process. In the fabrication of membrane structure, a 140 nm thickness Si_3N_4 hard mask was good enough to let dry etching achieving the depth to 800 nm in InP/InGaAsP layer. The $\text{SiH}_4/\text{NH}_3/\text{N}_2$ mixture gas was used to deposit dielectric hard mask on 300°C substrate at 35W plasma power in 100Pa pressure.

Before doing the deposit process, a surface treatment is necessarily. The wafers dip into BOE solution for few seconds to remove the negative oxide from InP. After that, put the wafers into acetone solution and use the ultra-sonic vibrator to clean the particles on surface. The surface treatment here is very important owing to a series depositing and etching processes later.



3.2.2. Photonic Crystal Patterns Definition

The photonic crystal patterns were defined by JEOL JSM-6500F electron-beam lithography (EBL) system. The EBL system is a field-emission scanning electron microscope, which employs a schmasky type fields-emission gun for the electron source and state-of-the-art computer technology for high-resolution image observation. The system had been modified with NPGS (Nanometer Pattern Generation System). It provides a user-friendly environment for the delineation of complex structures using a commercial electron microscope. It can easily write patterns on wafer by CAD file. The resolution of EBL system is about 1.5 nm for 15KV SEM and 20 nm for lithography. Accelerating voltage of electron-beam is from 0 KV to 30 KV. And the electron resister will be developed above 100 μA electron-beam.

At first, a A5 polymethylmethacrylate (PMMA) resist layer is spun on the sample by two spinning steps, 1000 rpm for 10 seconds and 4000 rpm for 25 seconds, respectively. Then, the sample was put on a 180°C hotplate for 90 seconds in order to do the soft-bake process. The PMMA layer is approximate to 300 nm in this recipe. If a smaller radius of air hole is needed, a thinner thickness of PMMA is better for development. The A3 PMMA can be spun about 100 nm thickness on the sample. After the soft-bake process, the smoothness of PMMA must be checked by naked eyes. The smoothness was determined by gloss from the sample.

Dosage of electron-beam is an important issue for a sample in EBL. There are two ways to test the dosage of electron. First, break one sample into two parts. One of the sample be used for testing wide range dosage and another of that is used to write the PC patterns in best dosage which we tested from the former sample.

Second, in the case for a sample that can not be broken, testing and writing process will be in the same wafer. After the testing process, we choose the best electron dosage from optical microscope (OM) or scanning electron microscope (SEM). Then, using acetone solution to remove the PMMA and repeat the same steps to write again in the same position.

Certainly, choosing the proper electron dosage is the key point to write good patterns on sample. As shown in Figure 3.2, the testing patterns write in wide range dosage. Then, deposit a thin Pt layer on the sample and use the SEM system to choose the better dosage. If you are an experienced user in EBL system, using the OM can also determine the proper dosage correctly. In Figure 3.2 (a) (b), there were still some residues of PMMA inside the air holes and the shape of holes were not good for PCs.

Those effects are causing to the insufficient electron dosage on sample. Oppositely, the shapes of air holes are closely to a circle and electron dosage is sufficient that there has no residue of PMMA inside the air holes.

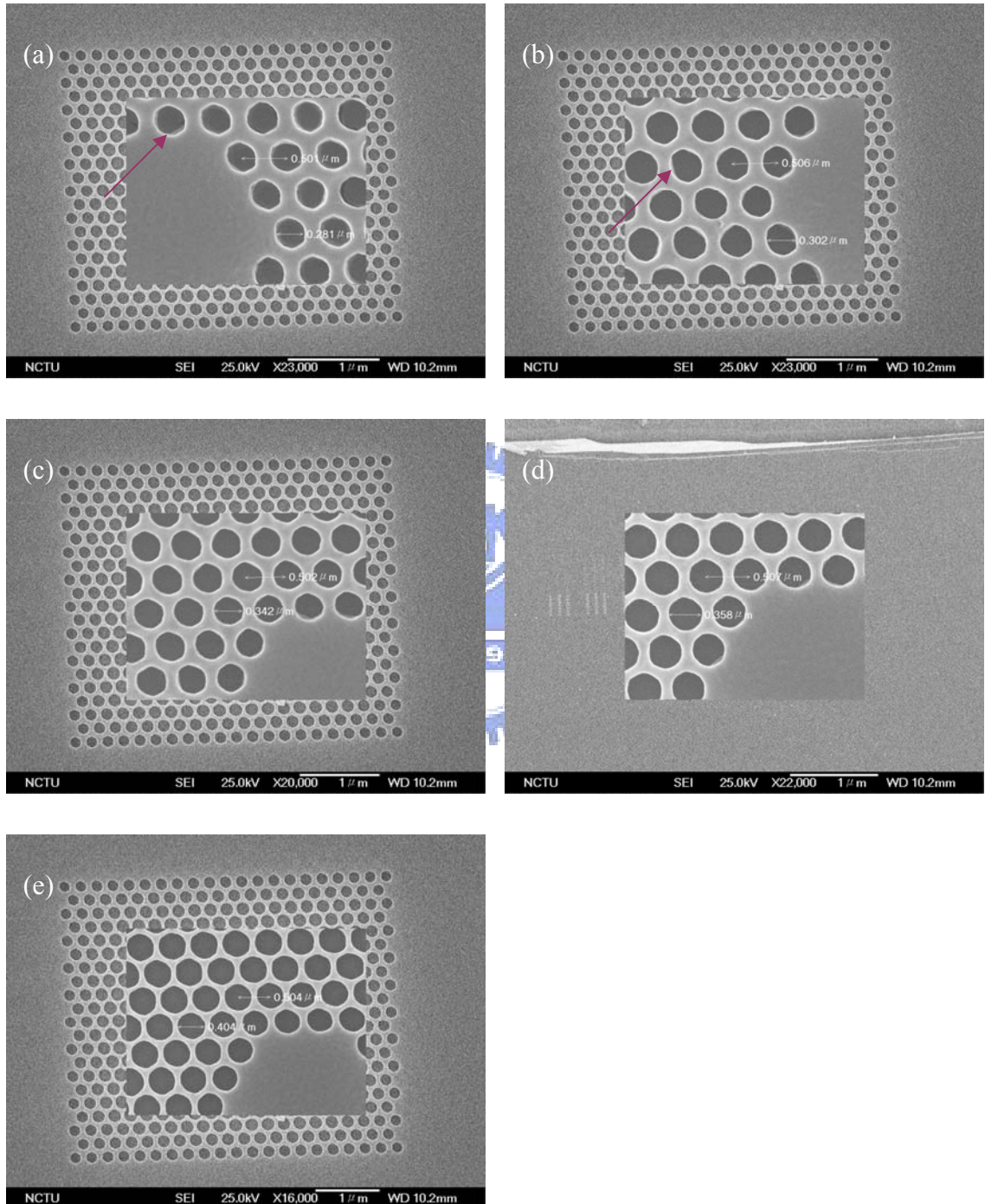


Figure 3.2 The illustrations are the same CAD pattern of triangular lattice PC microcavity laser with different electron beam dosage (a) 1.2 fC (b) 1.4 fC (c) 1.6 fC

(d)1.8 fC (e)2.1 fC. Obviously, the PCs holes in larger dosage are more circular than that in smaller one. There were still some residues of PMMA inside the air holes in (a) (b) because of the insufficient for electron dosage.

The proper air holes in PCs were appearance at a slightly overdose condition. In the design, therefore, the radius dimension in CAD files must smaller than the expected one about 20 nm. The inner-most air hole in microcavity, furthermore, is another issue in CAD design. Because of the mechanism in EBL system, the inner-most air holes were slightly smaller than others. This problem can also get a solution in lager radius design to inner-most air hole in CAD files.

There are many complicated steps in the EBL system. Before the writing process, every step must be checked carefully; otherwise, one mistake will turn all the previous labor to nothing. Finally, in the development process, the sample is developed in MIBK solution at temperature between 24 to 25°C for 70 seconds. As the shown in Figure 3.3, the PMMA layer will cause deformation if the temperature of development solution is over to 28°C. After the development process, the sample was put into the IPA solution about 30 seconds for cleaning the residues.

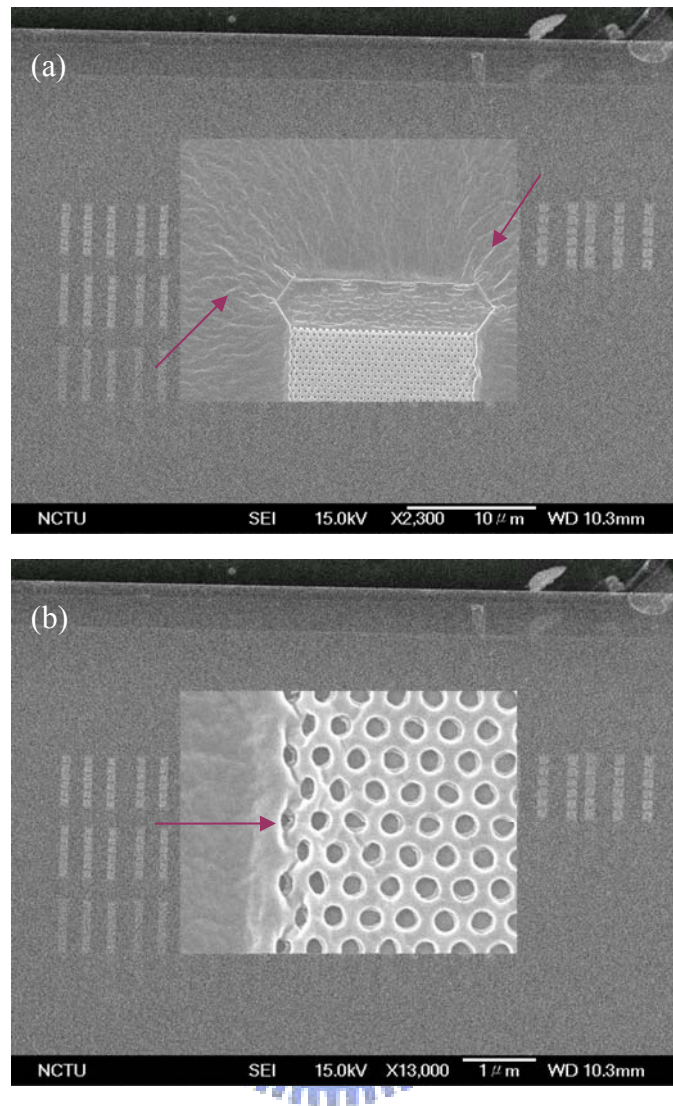


Figure 3.3 SEM top view of PC patterns after the PMMA development process. In the development process, the unusual control in temperature will cause (a) the creased PMMA surface and (b) distorted circle at the edge of PCs.

3.2.3. Patterns Transfer

After the patterns defined by EBL system, the patterns transfer process will be introduced as follows. For transferring PC patterns into InP layer, an Oxford Instruments Plasma Technology Plasmalab 100 inductively coupled plasma reactive ion etching (ICP/RIE) system was used. Si_3N_4 hard mask was etched by CHF_3/O_2 mixed gas in RIE

mode dry etching. Before the hard mask etching, the sample was etched by O_2 plasma firstly in order to clean the residual PMMA in air holes. The Si_3N_4 etching environment recipes are 150W RF power and 55 mTorr at $20^\circ C$ with gas flow rate CHF_3 and O_2 is 5 sccm and 50 sccm, respectively. The etching rate in CHF_3/O_2 mixed gas is about 1.5 nm/s in average and the selectivity ratio to PMMA is 8.

After the patterns transfer to Si_3N_4 layer, use the O_2 plasma to remove the PMMA layer. Checking the transferred PC patterns by high performance OM is one of the indispensable steps. During the time to check the patterns, ICP/RIE system can be set heating up to $150^\circ C$. If the patterns are good enough, keep doing the next process. Or else, the sample still can redo from Si_3N_4 depositing process. InP/InGaAsP MQWs layer was etched by $H_2/CH_4/Cl_2$ mixed gas in ICP mode dry etching. The MQWs etching environment recipes are 73W RF power, 1000W ICP power and 4 mTorr at $150^\circ C$ with gas flow pressure H_2 , CH_4 , and Cl_2 is 0.8, 0.4 and 0.3 mTorr, respectively. The etching rate in $H_2/CH_4/Cl_2$ mixed gas is 5.5 nm/s in average and the selectivity ratio to Si_3N_4 is 6. In Figure 3.4, it shown a side view SEM picture of PC patterns transferred to MQWs by a series of ICP/RIE dry etching processes. The top view OM picture of PC patterns is shown in Figure 3.5.

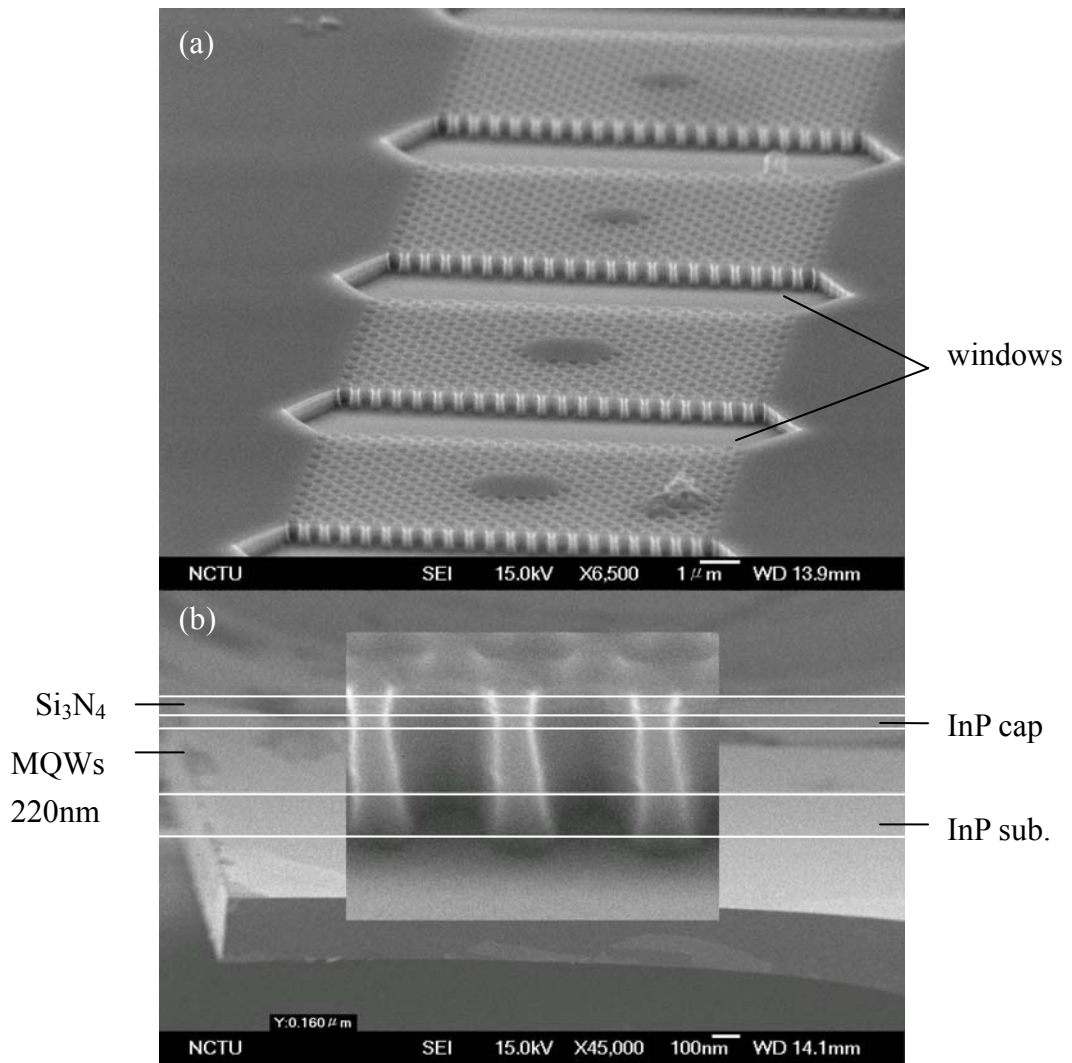


Figure 3.4 (a) A side view SEM picture of PC patterns transferred to MQWs by ICP/RIE dry etching processes. (b) The higher magnification of (a) from a window.

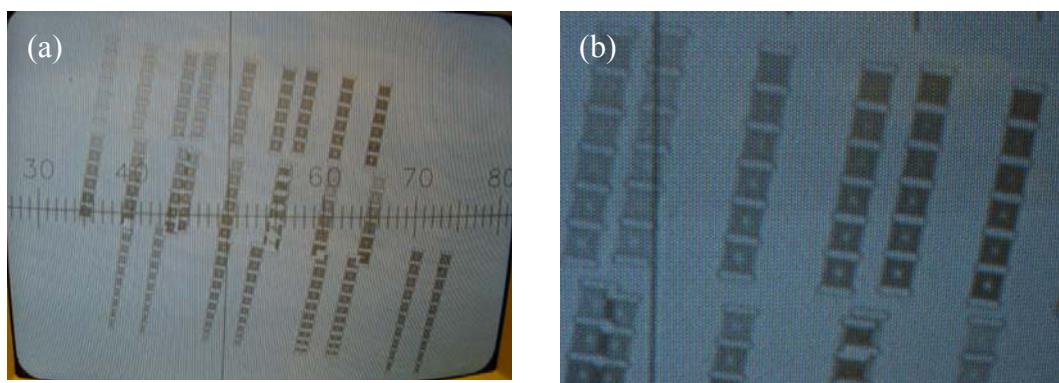


Figure 3.5 (a) A top view picture of PC patterns from high magnification OM system. (b) The higher magnification from (a).

There is a difference in two dry etching processes. In previous plasma technology, the etching profile is dependent on the gases flow rate. But in this ICP/RIE system, the dry etching profile is controlled by an auto-pressure control system. Briefly, we fixed the pressure causing by the gas flowing in chamber in each etching processes. That is because the fabrication pressure will change by the increasing particles that produced from every dry etching procedure. The mechanism of APC, therefore, could let the recipe of fabrication pressure be fixed in every etching process.

As shown in Figure 3.4 (b), the etching profile is not close to vertical as using the recipes that provided from factory. Therefore, we spend the few weeks to modify the proper recipes in the depth dry etching. In Figure 3.6, the etching profile in (a) is the initial recipes with 73W RF power and 0.3mTorr Cl_2 gas. Increase the RF power could modify the vertical profile and increase the Cl_2/CH_4 gas flow ratio could ease the horizontal sidewall etching in InP dry etching process. Obviously, the profile of Figure 3.6 (d) is better than others. Finally, well etching profile of the sample could be fabricated in our ICP/RIE dry etching system (Fig. 3.7).

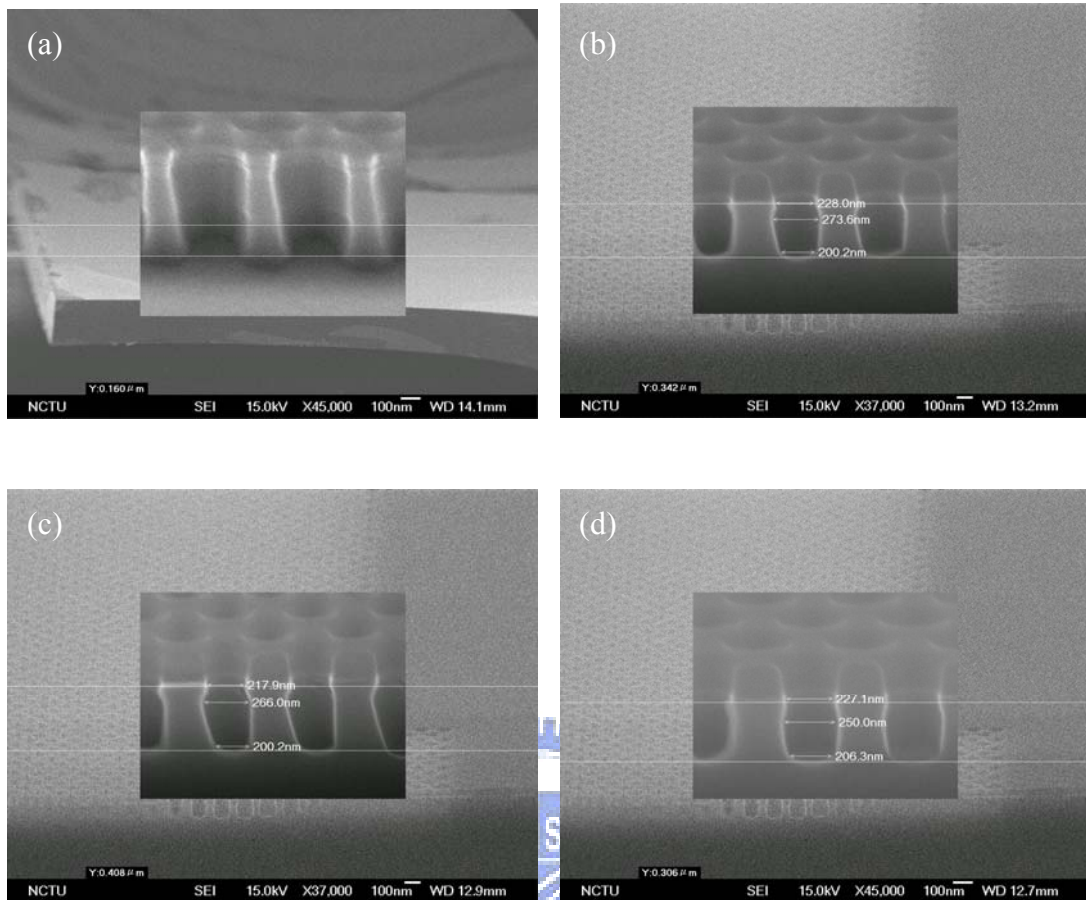


Figure 3.6 The dry etching profiles fabricated with the recipe of (a) 73W, 0.3mTorr (b) 73W, 0.4mTorr (c) 85W, 0.3mTorr (d) 85W, 0.4mTorr in RF power and the flowing pressure of Cl_2 gas, respectively.

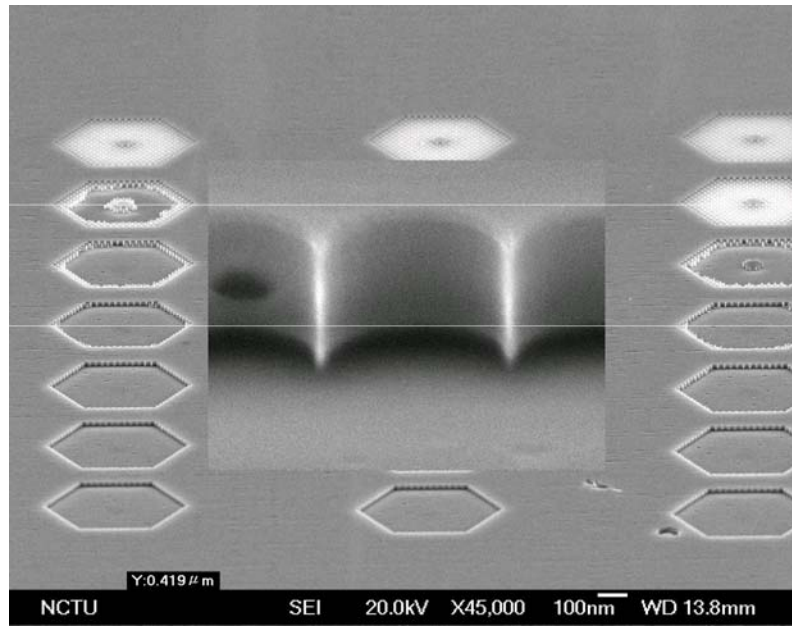


Figure 3.7 A side view of PCs with modified etching recipes in ICP/RIE dry etching process.

3.2.4. Substrate Undercut

In order to fabricate the membrane structure, the InP substrate below the MQWs should be removed. The undercut can be constructed by using a mixture solution with $\text{HCl} : \text{H}_2\text{O} = 4 : 1$ at 0°C for 9 minutes. This process also removes the 60 nm InP cap layer and smoothes the surface and the sidewall of the air holes. This process could be also regarded as a gentle wet etching process to reduce the optical loss caused by the surface roughness. Although wet etching process is anisotropic, the InP wet etching stops at 95° and 40° from $\langle -1, 0, 0 \rangle$ direction in the $(0, -1, -1)$ plane and the $(0, 1, -1)$ plane because of the material characteristic of InP as shown in Figure 3.8.

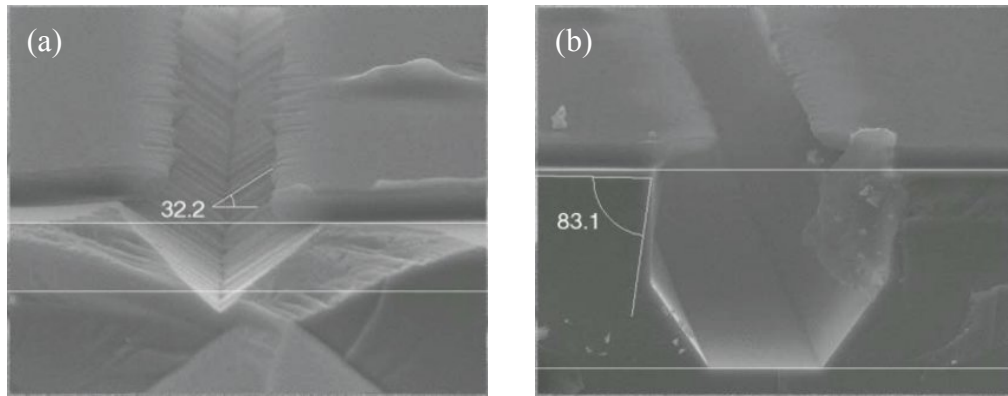


Figure 3.8 The illustration of (a) a 40° etching stop plane in (0, 1, -1) direction (b) a 95° etching stop plane in (0, -1, -1) direction of InP materials.

The undercut trench under the PC patterns can be formed for the larger air holes. For smaller radius of air holes, the wet etching results in a small wedge-shape undercut in each photonic crystal hole and the small wedges under every hole have no chance to meet each other at the corners of the etched feature (Fig. 3.9(b)). As Figure 3.9 (a) shown, therefore, the undercut trench of the pointed one can not be formed completely.

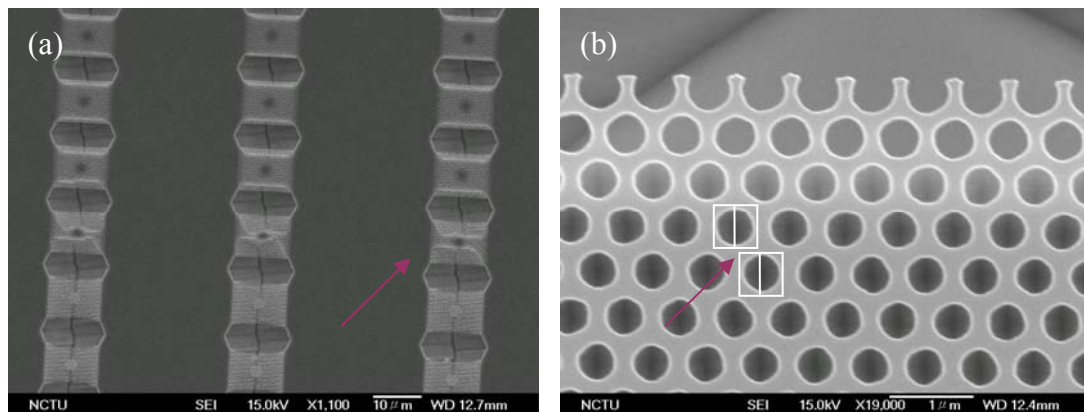


Figure 3.9 (a) The top view of a array of PC lasers. The lower PC lasers of the array have larger radius of air hole. (b) Small wedges under every hole have no chance to meet each other at the corners of the etched feature because the smaller radius of air holes.

We improved the yield in undercut process by the following presentation. In Figure 3.9 (a), a distorted black line was in one row of array. That is because the PC patterns did not parallel to the (0, 1, -1) direction of InP material exactly. Hence, the result could be modified in the EBL process. In Figure 3.10 (a), use the parallel line in SEM system to aim at (0, 1, -1) direction of the sample before electron-beam writing. Besides, change the mechanism in wet etching can also improve the yield. A magnetic rotor was put in the wet etching solution in order to keep the etching solution being refreshed at surface of sample. As the Figure 3.10 (b), a better performance of one array of 2D PC membrane lasers were demonstrated.

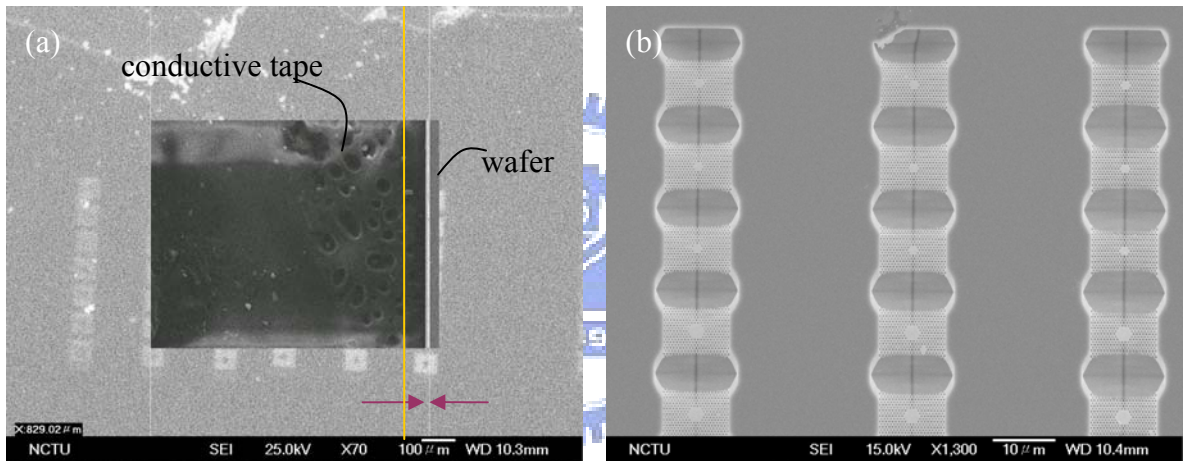


Figure 3.10 (a) The SEM of the aligning step before electron-beam writing. (b) A top view of an array of 2D PC lasers in modified undercut procedure.

3.3. Fabrication Results

The fabrications of the membrane structure PC lasers in detail were presented in the previous section. In this section, all of the demonstrated devices in my research will be introduced.

3.3.1. Triangular Periodic Photonic Crystal Lasers

The basic PC lasers we demonstrated in the early days of my researching. In Figure 3.11, there is one of the 7 missing air holes (D2) two-dimensional photonic crystal membrane laser. The 1, 7, 19 missing air holes lasers were also fabricated and discussed. D1 represent the meaning of 1 missing air hole and D2 represent 7, D3 represent 19 missing air holes, etc.

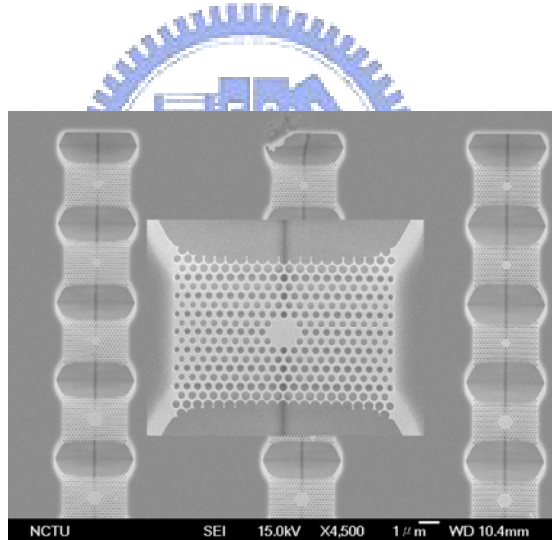


Figure 3.11 The top view of two-dimensional photonic crystal membrane lasers array. This microcavity is formed by 7 missing air holes.

3.3.2. Quasi-Periodic Photonic Crystal Lasers

In this section, we demonstrated the SEM pictures of some designed QPC lasers in our group, as shown in Figure 3.12. Dodecahedral QPCs was discussed mainly in my thesis. An oblique view of fabricated 12-fold QPC microcavity lasers which suspended

the membrane structure (Fig. 3.12(a)). Obviously, a V-shape trench was fabricated by an anisotropic wet etching. The line in V-shape trench can also be observed from the top view of 12-fold QPC membrane structure lasers (Fig. 3.12(b)). Higher magnification 12-fold QPC lasers were shown in the inset of Figure 3.12(b) with D2 (left) and D3 (right) microcavity. The 8-fold QPC lasers and the circular-periodic photonic crystal (CPC) lasers were presented in Figure 3.12 (c) and (d), respectively.

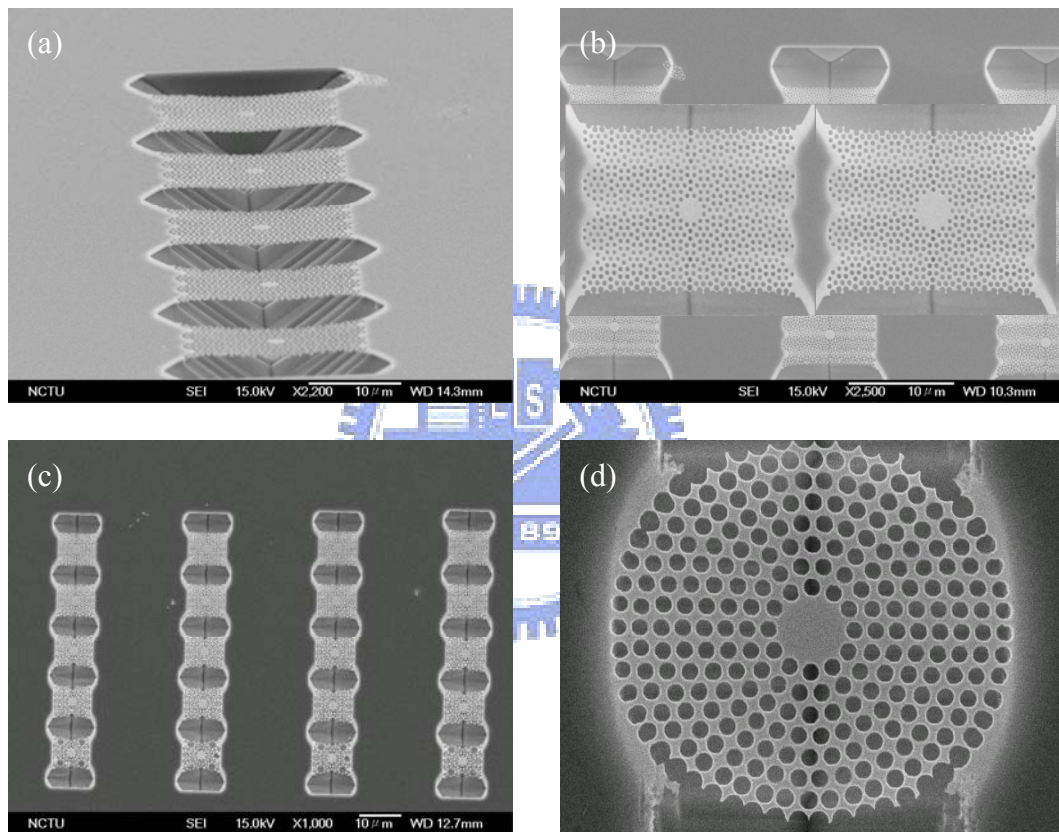


Figure 3.12 (a) The oblique view of fabricated QPC microcavity lasers suspended membrane structure. (b) The top view of 12-fold QPC membrane lasers array with D2 (left) and D3 (right) microcavity. (c) The top view of 8-fold QPC membrane lasers array with D2 microcavity. (d) The top view of circular PCs membrane lasers array with D2 microcavity.

3.3.3. Modified Quasi-Periodic Photonic Crystal Lasers

After the study in 12-fold QPC lasers, the resonance and lasing modes were characterized with some kind of WGMs. In order to reduce the resonance modes, the modified 12-fold QPC lasers were designed. As shown in Figure 3.13(b), one of the 12-fold QPC laser was modified by a designed central hole. Furthermore, the shifting of radius and lattice constant in the fabrication of EBL process were also discussed. The characteristic of these fabricated devices were being analyzed and discussed in chapter of measurement results.

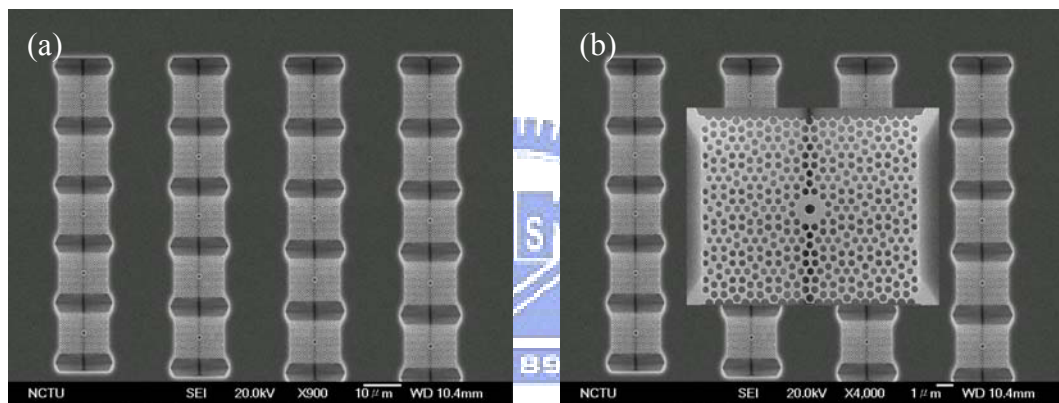


Figure 3.13 (a) A top view of 12-fold modified QPC membrane lasers array with D2 microcavities. (b) The higher magnification of one modified QPC laser from (a).

3.4. Conclusion

In Figure 3.14, there is an overview of fabrication processes of two-dimensional photonic crystal membrane structure lasers. In the following, there is a summary of introduced fabrication in this chapter. The epitaxial structure consisting of four 10 nm compressively-strained InGaAsP MQWs as the active layer with 1550 nm central wavelength is prepared. Then, a 140 nm silicon-nitride layer served as hard mask for latter etching process is deposited on the epitaxial wafer by PECVD system. And the PMMA layer is spin-coated on the Si₃N₄ layer. The PC or QPC patterns are defined on the PMMA layer by EBL and transferred to the Si₃N₄ layer by RIE process with CHF₃/O₂ mixed gas. Then the patterns are further transferred to MQWs by ICP dry etching with CH₄/Cl₂/H₂ mixed gas at 150°C. Finally, the membrane structure is formed by selective wet etching with the mixture of HCl and H₂O at 0°C.



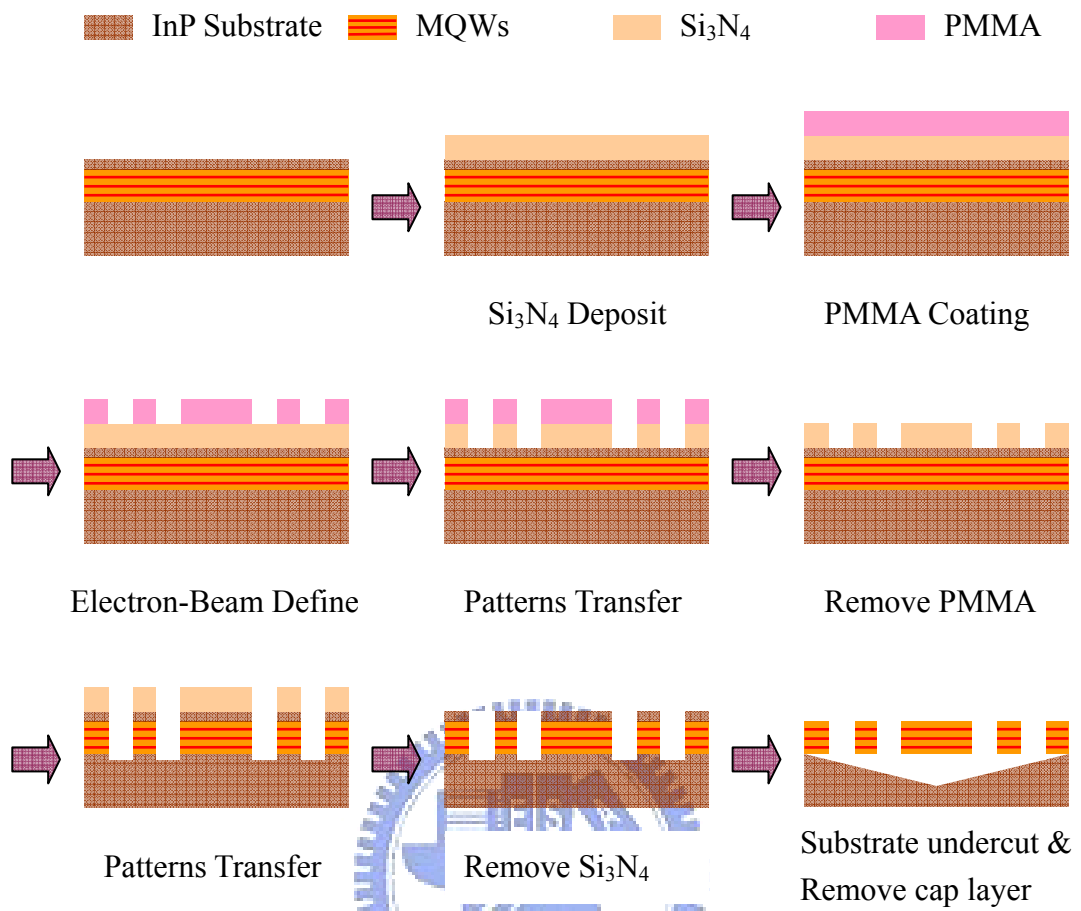


Figure 3.14 An overview of fabrication processes of two-dimensional photonic crystal membrane structure lasers.

Chapter 4 Fabrication of Wafer Bonding Structure

Photonic Crystal Lasers

4.1. Introduction

The basic design principles for asymmetry structure have been introduced in chapter 2. In this chapter, the fabrication procedures of asymmetry structure lasers in detail and the problems in process will be presented. In order to integrate the asymmetry structure with InP/InGaAsP material, wafer bonding technology is required. We have had tried lots of wafer bonding technologies in last two years on the purpose to support the later procedures. And the proper and modified fabrication processes will also be introduced in each section.

4.2. Fabrication of Photonic Crystal Lasers with DBR Bonding

The epitaxial structure of MQWs wafer for wafer bonding is shown in Figure 4.1. This structure is similar to the epitaxial structure for membrane fabrication. The same epitaxial structure consists of four 10 nm 0.85% compressively strained InGaAsP quantum wells which are separated by three 20 nm unstrained InGaAsP barrier layers. The wafer structure differences from membrane structure are one 40 nm InGaAs etching stop layer above InP substrate and two different InP cap layer above the MQWs. InGaAs etching stop layer is used to protect the MQWs during the removing InP substrate process. Two different InP cap layer were designed owing to prove the relation with the thickness of InP cap layer and the yield of wafer bonding.

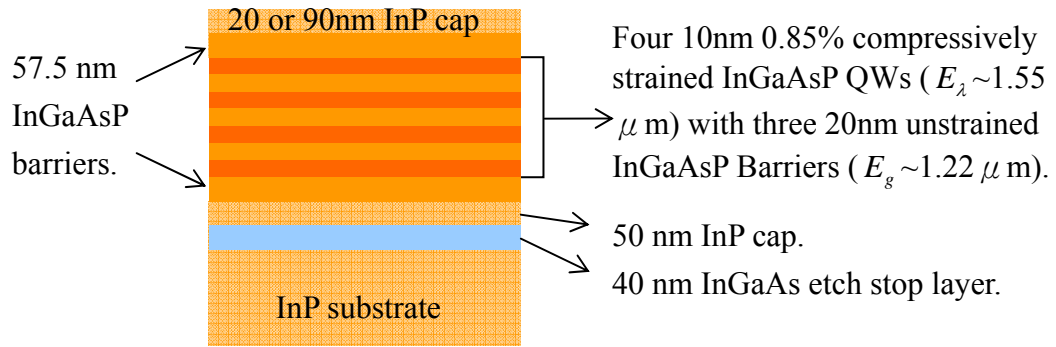


Figure 4.1 A illustration of epitaxial structure of InGaAsP QWs for wafer bonding structure lasers. InGaAs etching stop layer is used to protect the MQWs during the removing InP substrate process.

4.2.1. Preparation for Wafer Bonding

Before the wafer bonding process, a few of channel lines must be transferred on the InP cap layer in order to banish the steam from the joint surface of two wafers. If you did not do the channel lines, the wafer bonding process will being fail owing to the residual steam between two wafers. At first, a surface treatment is still required before the process. The wafers dip into BOE solution for few seconds to remove the negative oxide from InP. After that, put the wafers into acetone solution and use the ultra-sonic vibrator to clean the particles on surface. The sample was cleaned by D.I. water and put on the 120°C hot plate for 2 minutes. This drying step is preventing the residual steam to mix with the photoresist in the coating process. After drying the sample, use the N₂ gun to cool it down until achieving the room temperature.

AZ6112 positive photoresist is spun on the sample by two spinning steps, 1000 rpm for 10 seconds and 3500 rpm for 25 seconds, respectively. Then, the sample was put on a 90°C hotplate for 90 seconds in order to do the soft-bake process. The photoresist

layer is approximate to 1200 nm in this recipe. After the soft-bake process, the smoothness of PMMA must be checked by naked eyes. The smoothness was determined by gloss from the sample. The requirement for smoothness quality was not as high as EBL in this channel process. A mask aligner was used to define patterns on the wafer during 12.5 seconds without an attachment lens. After the exposure process, the sample was put into develop solution, AZ300, for 8 ~ 10 seconds and cleaned by the D.I. Water. Before wet etching process, the sample was put on a 120°C hotplate for 2 ~ 3 minutes to do the hard-bake process.



Figure 4.2 A top view of two bonding structure samples after channel patterns defined.

When we doing the process of patterns defined, all of the wafer bonding fixture could be cleaning with acetone solution in the same time. An appropriate cleaning step for the fixture is very important for every wafer bonding process. After the channel development, the sample was dip into a solution $\text{HCl} : \text{H}_3\text{PO}_4 = 1 : 1$ for 10 ~ 20 seconds. Then, remove the photoresist with acetone solution. A channel defined sample was completed as shown in Figure 4.2. The sample and DBR or Sapphire wafer were cleaned in the same acetone solution for 5 minutes. After that, two wafers were cleaned

in the same cup by continuous D.I. Water rinse for 5 minutes. After the cleaning process, two wafers were stick together face to face in the D.I. Water. Blowing the water for drying the stuck sample, and checking two wafers were stuck by Van der Waals force. As the Figure 4.3 shown, the stuck sample was clipped on the wafer bonding fixture.

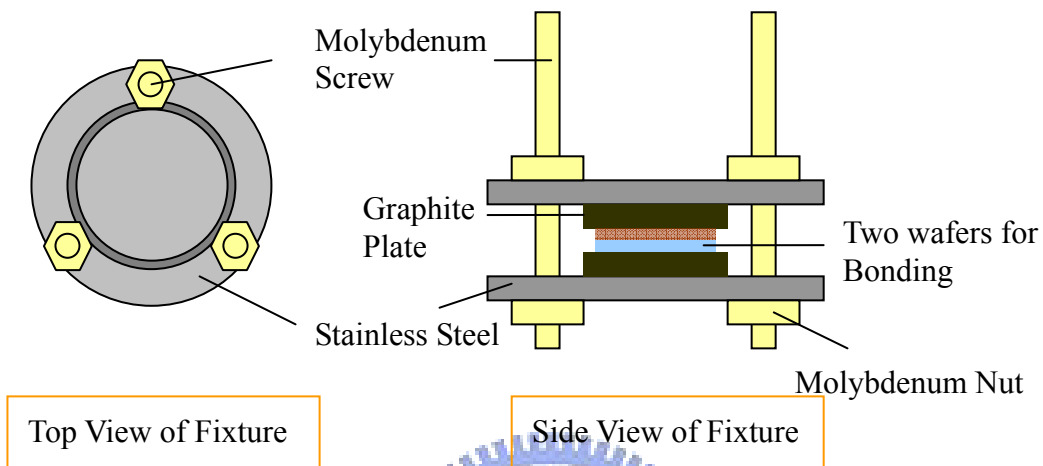


Figure 4.3 The scheme of top view and the side view of wafer bonding fixture. A stuck wafer was clipped on the wafer bonding fixture.

4.2.2. Wafer Bonding System

As shown in Figure 4.4, the wafer bonding fixture was put into the center of furnace. 3 atm N_2 gas and mechanical pump were used for purge the air to vacuum in furnace. Continue doing this step for several times then pump out the N_2 gas to high vacuum for 5 minutes. Vent 1 atm H_2 gas into the vacuum furnace for wafer bonding gas. After that, use the PID controller to heat the furnace for different bonding wafers. In the case for DBR bonding, the sample is heated to $600^\circ C$ in 90 minutes and hold the temperature for 60 minutes with the H_2 gas to prevent the occurring of native oxide. Moreover, in the case for Sapphire bonding, the sample is heated to $450^\circ C$ in 100 minutes and hold the temperature for 30 minutes. Finally, the annealing process was that

let the furnace cool down naturally to room temperature. Annealing process always spent for 10 hours above.

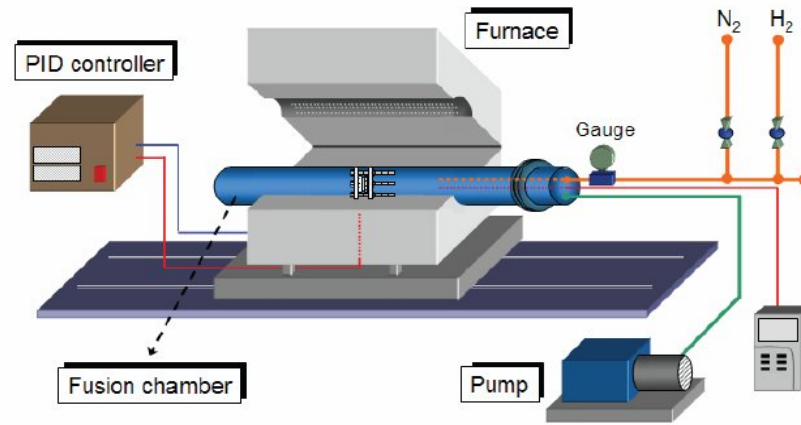


Figure 4.4 A illustration of the wafer bonding (fusion) system.

The different thermal expansion coefficient of stainless steel and molybdenum material is the main principle of wafer-bonding process. Owing to the different thermal expansion coefficient, high pressure between the stainless steels was formed at high temperature. Generally, this pressure will also up to several MPa during the wafer bonding process. In Table 4.1, the thermal expansion coefficients of stainless steel and molybdenum with different temperatures are listed.

Table 4.1 The thermal expansion coefficients of stainless steel and molybdenum material with different temperatures.

Materials\Temperature	373K	600K	800K	1000K
Molybdenum (Mo)	5.42	5.82	6.2	6.71
Stainless Steel	17.2	17.8	18.4	19.3

Because of the high temperature and high pressure be occurred in furnace, the interface of two wafers would have a chemical reaction to form the atomic covalent bond. That is the main mechanism of wafer bonding process. Furthermore, the function of graphite plate is to prevent the bonding reaction between wafer and stainless steel. After the proper time for annealing, two wafers were bonded together as shown in Figure 4.5.

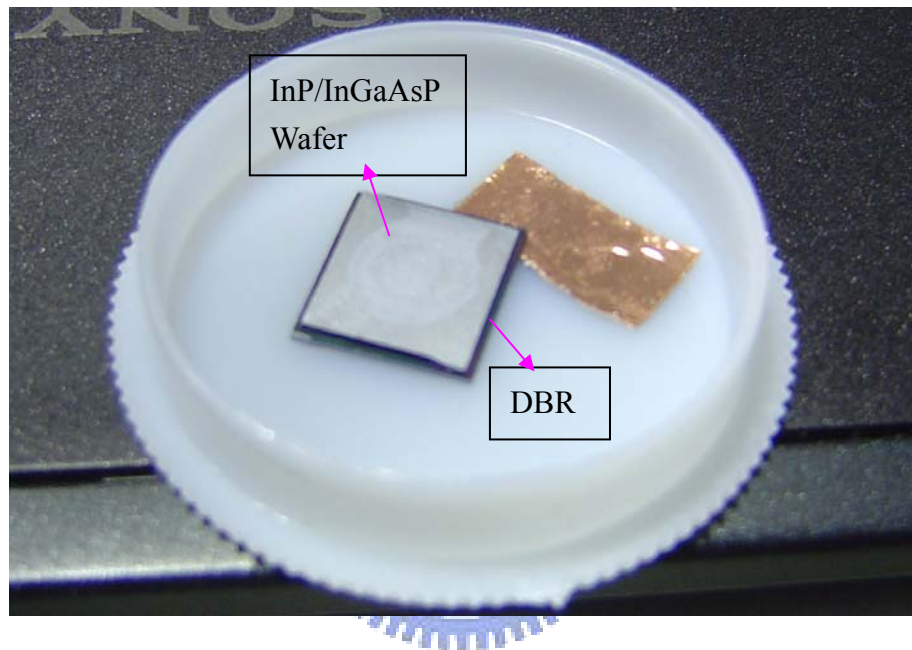


Figure 4.5 The picture shows a tilt sample after wafer bonding process. The upper layer of sample is a InP/InGaAsP QWs wafer and the lower one is a DBR wafer.

4.2.3. Substrate Removal

After the wafer bonding process, the upper layer of InP substrate will be removed by wet etching. As the wet etching process in Chapter 3, a magnetic rotor was put in the wet etching solution in order to keep the etching solution being refreshed at surface of sample. But the main reason for using a magnetic rotor is to move the bubble on the etching surface in wet etching process. The bubble will cause the QWs surface non-uniform seriously.

The bonded sample was fixed by clips and put into a $\text{HCl} : \text{H}_2\text{O} = 4 : 1$ solution for 30 minutes or a $\text{HCl} : \text{H}_2\text{O} = 3 : 1$ solution for 50 minutes. After that, the etching stop layer was etching by a $\text{H}_3\text{PO}_4 : \text{H}_2\text{O}_2 : \text{H}_2\text{O} = 1 : 1 : 8$ solution for 10 seconds. Finally, remove the 50 nm InP cap layer by the same $\text{HCl}/\text{H}_2\text{O}$ solution for 5 seconds. The smooth and glossy MQWs with DBR substrate wafer was demonstrated as shown in Figure 4.6.

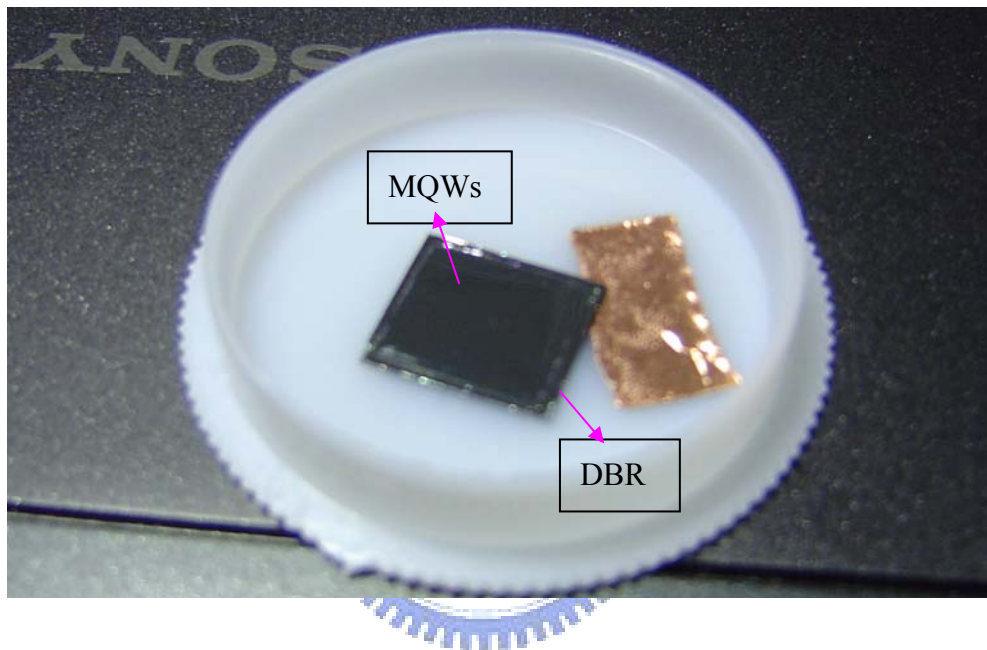
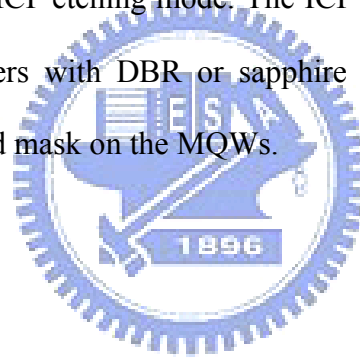


Figure 4.6 The picture shows a tilt sample after remove InP substrate. The smooth and glossy surface is the InGaAsP MQWs with DBR substrate.

4.2.4. Photonic Crystal Patterns Definition and Transfer

Up to here, we finished the wafer bonding process. The quality of the bonded wafer can be check from the photoluminescence (PL) system. The purpose of following steps is going to define the PC patterns on the surface of bonded wafer. The procedures of patterns definition were almost similar to the processes in membrane structure PC lasers. Certainly, the following processes in wafer bonding structure were introduced briefly and pointed out the difference in membrane structure.

After the PL check, a smooth and best enhancement area was being chosen for PCs definition. We deposited a 300 nm thickness Si_3N_4 layer as an etch mask by PECVD process. The thicker Si_3N_4 than 140 nm is owing to against the longer dry etching time. A 300 nm thickness of PMMA layer was spun on Si_3N_4 layer, and the PC microcavity patterns were written by EBL system. In the EBL process, we use the second method of dosage testing which introduced in Chapter 3. For transferring PC patterns into MQWs layer, the ICP/RIE system was used. The Si_3N_4 hard mask was etched by CHF_3/O_2 mixed gas in RIE mode dry etching, and then $\text{CH}_4/\text{Cl}_2/\text{H}_2$ mixed gas is used to transfer the patterns into MQWs at 150°C for 40 seconds in ICP etching mode. Then, the Ar/SiCl_4 mixed gas is used to transfer the PC patters into DBR (GaAs/InGaAs) substrate at 20°C for 4 minutes in ICP etching mode. The ICP and RF power is 350W and 30W, respectively. The PC lasers with DBR or sapphire structure was demonstrated after removing the residual hard mask on the MQWs.



4.3. Fabrication Result & Conclusion

In Figure 4.8, there is an overview of fabrication processes of two-dimensional photonic crystal wafer bonding structure lasers. In the following, there is a summary of introduced fabrication in this chapter. The epitaxial structure consisting of four 10 nm compressively-strained InGaAsP MQWs as the active layer with 1550 nm central wavelength is prepared. After the channel lines defined, the sample is bonded to the DBR or sapphire substrate by wafer fusion system in H₂ gas at 600 or 450°C, respectively. The InP substrate and 20 nm etching stop layer will be removed after the wafer bonding process. Then, a 300 nm silicon-nitride layer served as hard mask for latter etching process is deposited on the epitaxial wafer by PECVD system. And the PMMA layer is spin-coated on the Si₃N₄ layer. The PC or QPC patterns are defined on the PMMA layer by EBL and transferred to the Si₃N₄ layer by RIE process with CHF₃/O₂ mixed gas. And the patterns are further transferred to MQWs by ICP dry etching with CH₄/Cl₂/H₂ mixed gas at 150°C. The patterns are further transferred to DBR substrate by ICP dry etching with Ar/SiCl₄ mixed gas at 20°C. Finally, the wafer bonding structure laser is formed by removing the hard mask on MQWs surface.

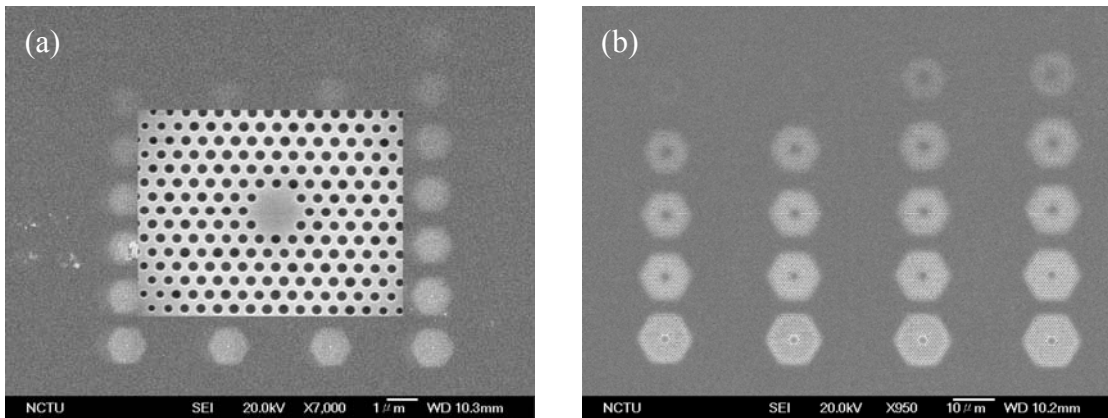
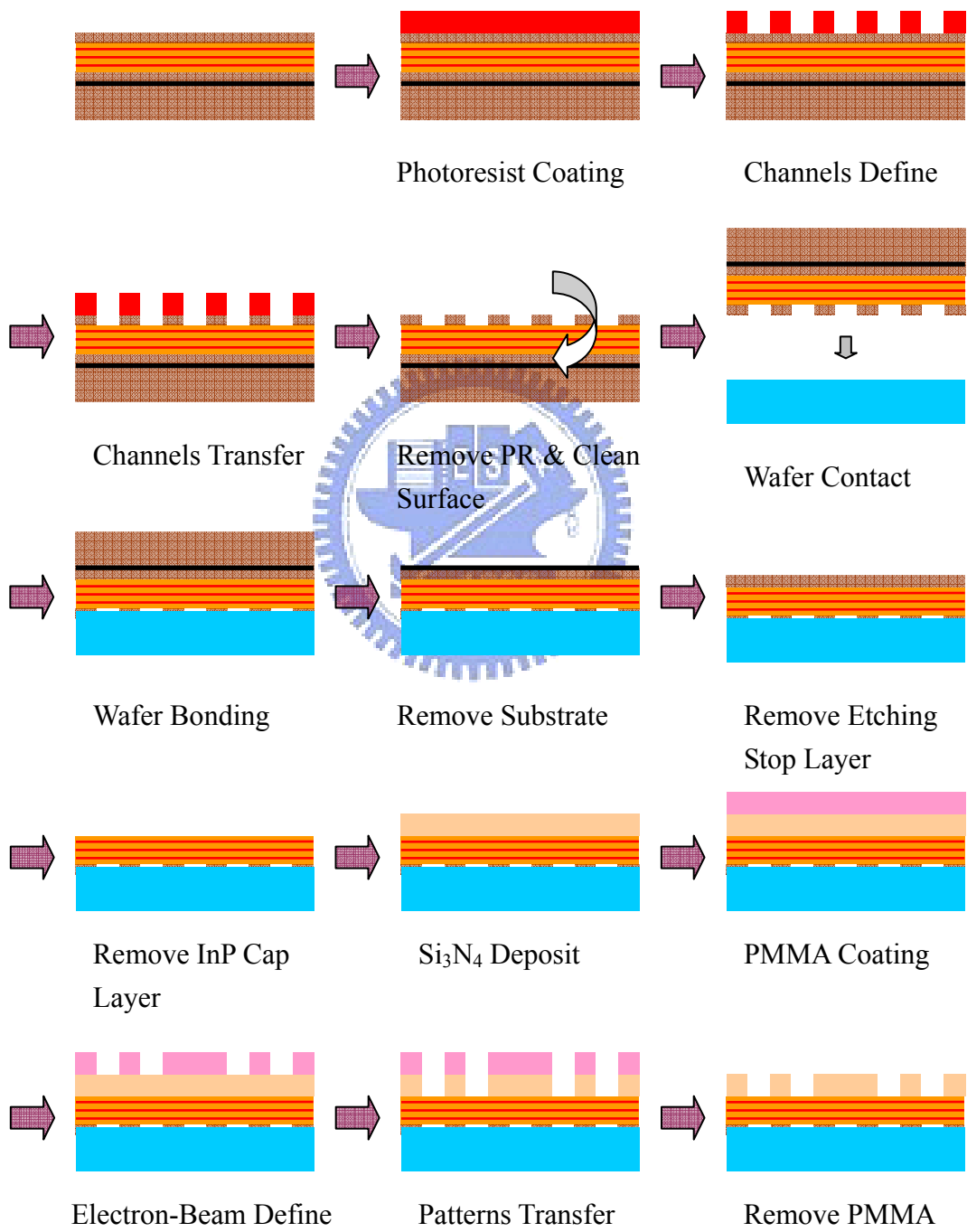
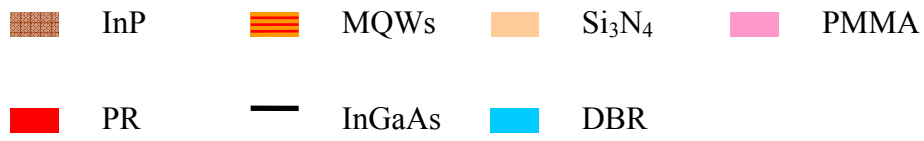


Figure 4.7 The SEM top view of the (a) D2 (b) D3 PC lasers bonding with DBR wafer.



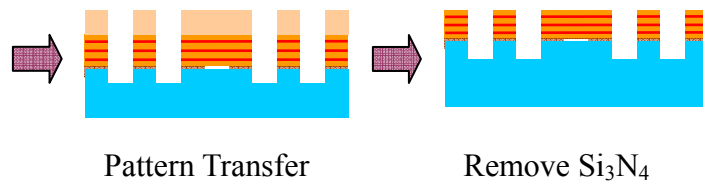


Figure 4.8 An overview of fabrication processes of two-dimensional photonic crystal with DBR or Sapphire wafer bonding.



Chapter 5 Measurement Results

5.1. Introduction

In order to measure the characteristics of the epitaxial materials and two-dimensional photonic crystal microcavities, a micro-PL system with sub-micrometer scale resolution in

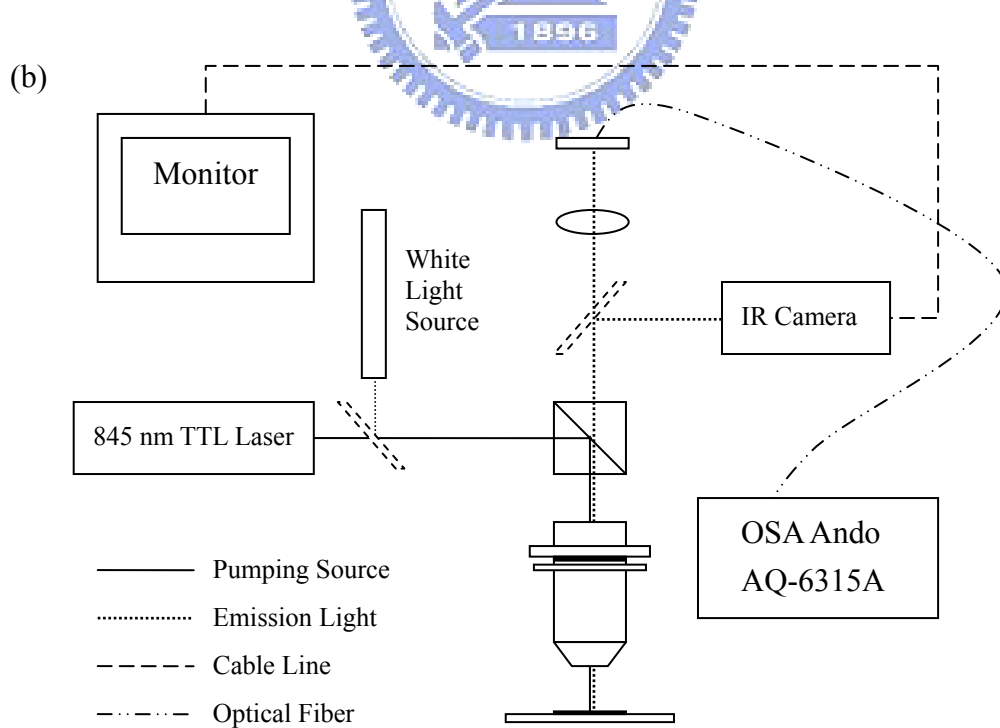
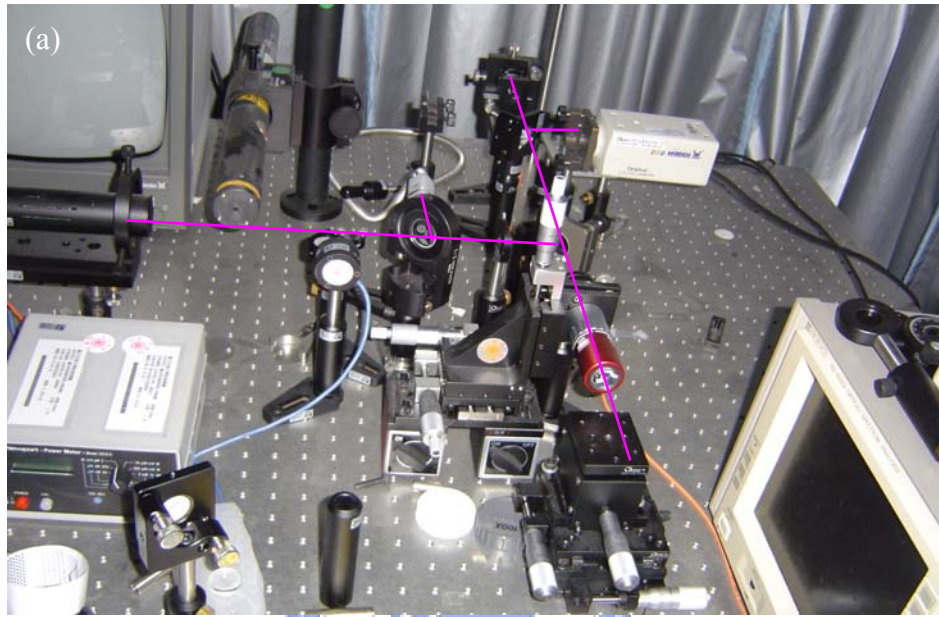
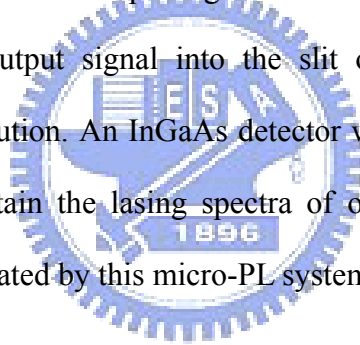


Figure 5.1 (a) The picture shows our micro-PL system. (b) The scheme illustrates the configuration of (a).

space and sub-nanometer scale resolution in spectrum is necessary. The simple configuration and photo of the micro-PL system are shown in Fig 5.1 (a) and (b), respectively.

In this system, an 845 nm TTL laser is used as the pump source. This TTL laser can be used in pulse operation and continuous-wave (CW) operation by switching a function generator. The pump beam is reflected into a 50x long working distance NIR objective lens which is mounted on a 3-axis stage with numerical aperture of 0.5 by a 50/50 beam splitter. The 48% reflection in angle 45° of the splitter for 845 nm wavelength is confirmed. And the pump beam is focused to a spot with 2 μm to 3 μm in diameter by the objective lens.

The objective lens collects the output light from the top of the sample. We use a collective lens to focus the output signal into the slit of our spectrum analyzer, Ando AQ-6315A, with 0.05 nm resolution. An InGaAs detector with good responsibility from 900 nm to 1600 nm is used to obtain the lasing spectra of our devices. All of the following measurement results were estimated by this micro-PL system.



5.2. Basic Lasing Characteristics

In this section, we will show some basic characteristics of two-dimensional photonic crystal lasers including lasing spectrum, L-L curve, mode polarization, and mode hopping properties in membrane and wafer bonding structure. All measurements are done at room temperature by our micro-PL system.

5.2.1. Measurement Results from Membrane Structure

The lasing spectrum well above threshold of a typical two-dimensional photonic crystal laser with 0.5 % duty cycle at 0.2MHz repetition rate is shown as following figure. In Figure 5.2, the lasing wavelength is 1560.3 nm and full-width half-maximum (FWHM) is 0.15nm. The side mode suppression ratio (SMSR) is about 30 dB in this lasing spectrum. And the inset of Figure 5.2 indicated near-threshold lasing spectrum at 0.155 mW. In Figure 5.3, the lasing wavelength is 1545.6 nm and full-width half-maximum (FWHM) is 0.18nm. The SMSR is about 15 dB in this lasing spectrum. And the inset of Figure 5.3 indicated near-threshold lasing spectrum at 0.312 mW. Obviously, we can tune the lasing wavelength to our purpose, 1550 nm, either D2 or D3 QPC microcavity lasers.

Comparing to D2 and D3 microcavity lasers, the FWHM of D3 is generally broader than that of D2 in experiment. Therefore, the quality (Q) factor of D2 microcavity is higher than D3 one. That is because the different lasing mode in those microcavity although the bigger cavity has a longer photon life time. As we simulated in Chapter 2, this lasing mode in D2 QPC laser was demonstrated to a WGM. The theory of WGM was also introduced that a WGM can enhance higher Q factor and lower threshold. In the experiment results, the Q factor of D2 and D3 QPC lasers is about

10,400 and 8,600, respectively. The Q factor is estimated from the measured line-width near the transparency pump power. Consequently, a higher Q factor can be obtained from D2 QPC laser owing to its WGM lasing mode.

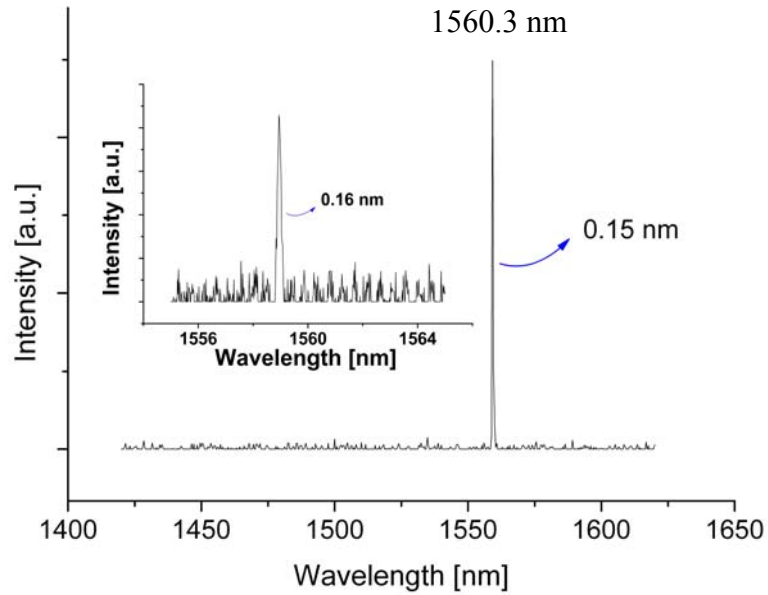


Figure 5.2 A typical lasing spectra above threshold of a two-dimensional D2 microcavity QPC laser. The FWHM of this lasing mode is 0.15 nm at 2.86 mW pump power and the inset indicated near-threshold lasing spectrum at 0.155 mW.

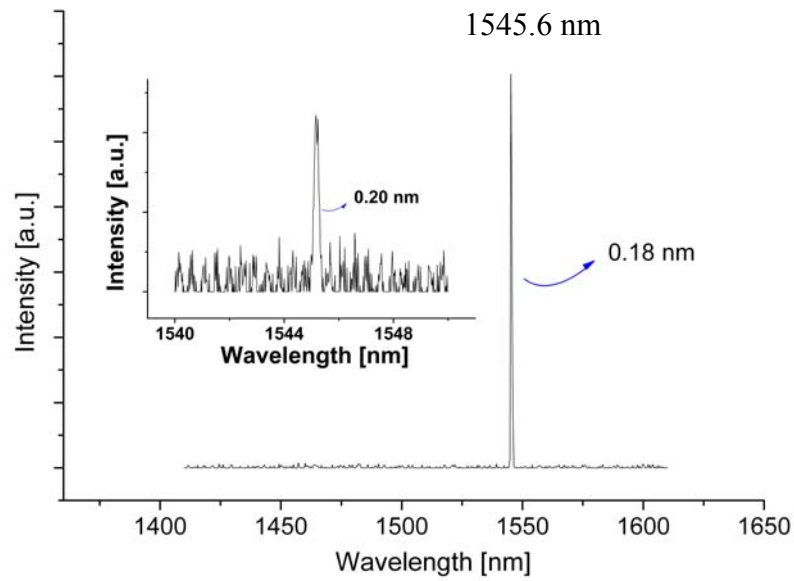


Figure 5.3 A typical lasing spectra above threshold of a two-dimensional D3 microcavity QPC laser. The FWHM of this lasing mode is 0.18 nm at 3.26 mW pump power and the inset indicated near-threshold lasing spectrum at 0.312 mW.

The lasing spectra of one QPC laser were illustrated at below threshold condition to 20 times threshold pumping power in Figure 5.4. Collating all of the lasing spectra to the PL pumping power, the L-L curve of one laser device can be illustrated, as shown in Figure 5.5, 5.6. The characteristics of D2 and D3 QPC microcavity were shown in Figure 5.5. Obviously, the smaller cavity, D2, was first rolling off around 2 mW by a rather serious thermal effect to the lager one.

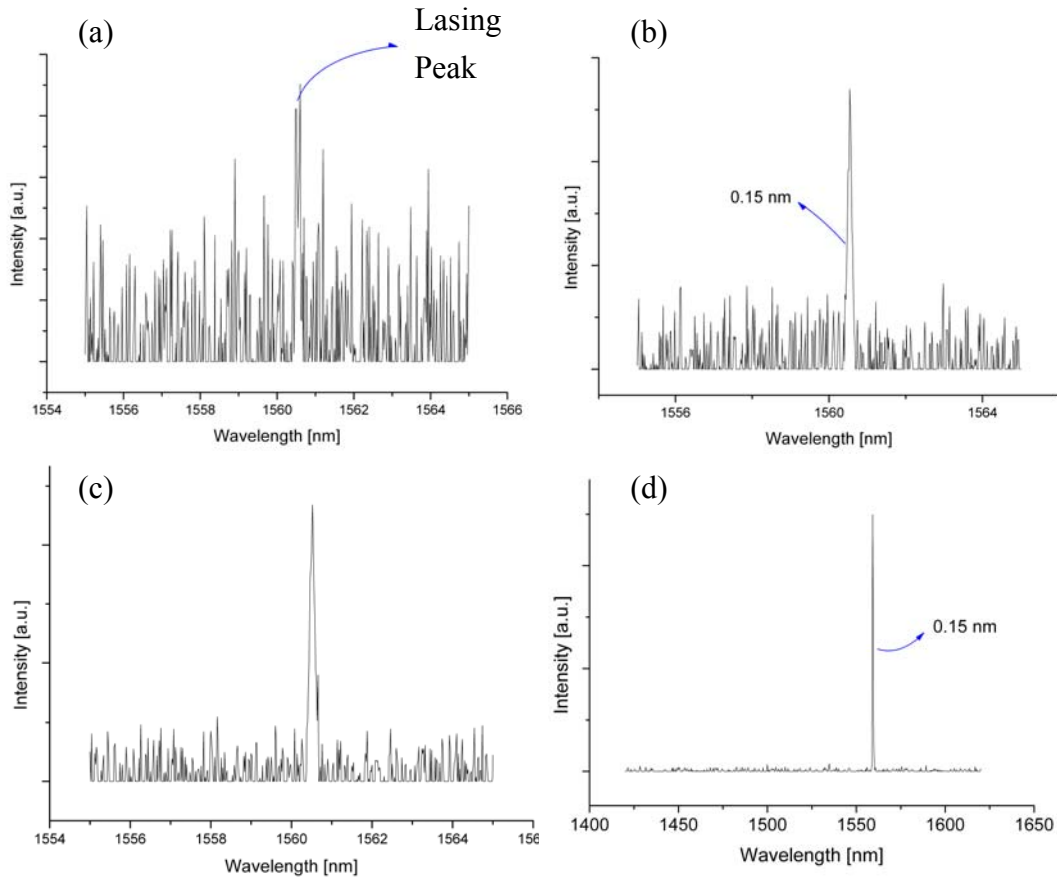


Figure 5.4 The illustration of the lasing spectra of one QPC laser at the (a) below threshold (b) near threshold (c) above threshold (d) 20 times threshold pump power.

The insert of Figure 5.5 shows the characteristic of QPC lasers at near threshold condition. It indicated the ultra-low threshold pump power, 0.186 mW, from a D2 QPC laser; and slightly higher threshold, 0.246 mW, measured from a D3 QPC laser. The thresholds of triangular lattice PC lasers which were fabricated in the same wafer are mostly about 0.6 mW and 0.3 nm FWHM (Fig. 5.6). As the mirror of micro-cavity, more isotropic and efficient PBG confinement can be provided by QPC, which leads the D2 QPC laser to a lower threshold. The quality factor of D2 QPC and triangular lattice PC is over 10,000 and 3,500, respectively. The higher quality factor is because of the WGM.

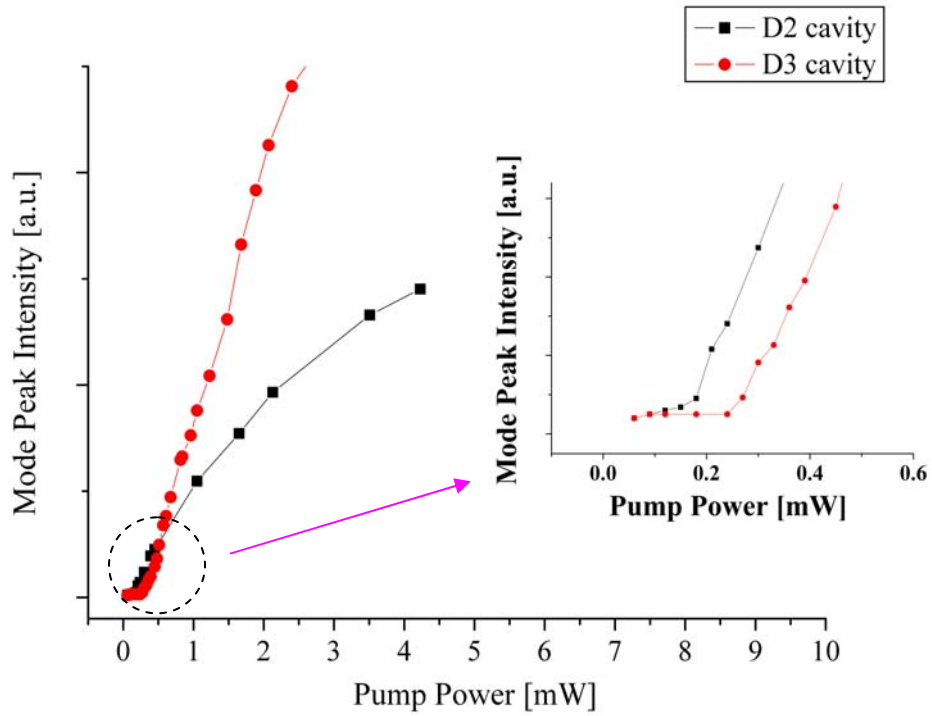


Figure 5.5 The L-L curve of two-dimensional QPC lasers with D2 and D3 microcavity. The thresholds are estimated to be 0.186 and 0.246 mW input pump power, respectively.

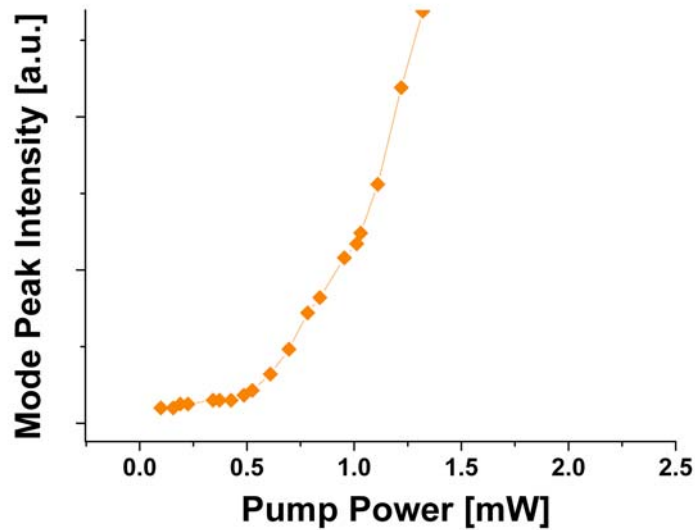


Figure 5.6 The L-L curve of two-dimensional triangular lattice PC laser with D2 microcavity. The threshold is estimated to be 0.6 mW input pump power.

In order to tune the lasing wavelength for our purpose, we fabricated the array with varying lattice parameters constant of the PC/QPC patterns such as the r/a ratio and the lattice constant. The SEM pictures of the 2D PC/QPC laser array are shown in Chapter 3 and 4. The lasing wavelength can be tuned by different lattice constants with a fixed r/a ratio. As shown in Figure 5.7, the lasing wavelengths of two laser arrays with the varying lattice constant and the fixed r/a ratio 0.36 and 0.39. There is also a mode hopping phenomenon in 12-fold QPC lasers as in triangular lattice PC lasers (Fig 5.7). This phenomenon is caused by the variation of the alignment between the PL gain peak and the resonance modes. The upper resonance mode is the main lasing mode and the lower one is the second lasing mode in 12-fold QPC lasers. The threshold is around 0.2 mW and over than 1mW in 12-fold QPC lasers, respectively. That is another way to prove WGM by the characteristics of thresholds. In Figure 5.8, the corresponding lasing wavelengths are denoted by solid circles. The measured data quite agree with the simulated results and we can identify the corresponding lasing modes.

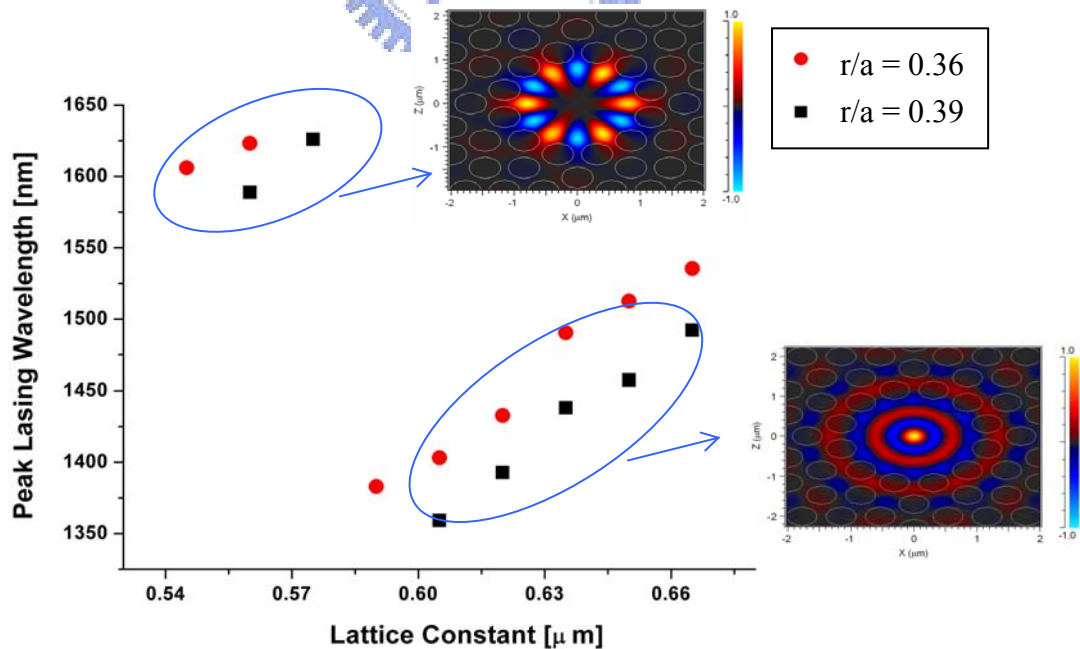


Figure 5.7 Lasing wavelength tuning caused by varying lattice constants. The inserts illustrate its corresponding lasing modes.

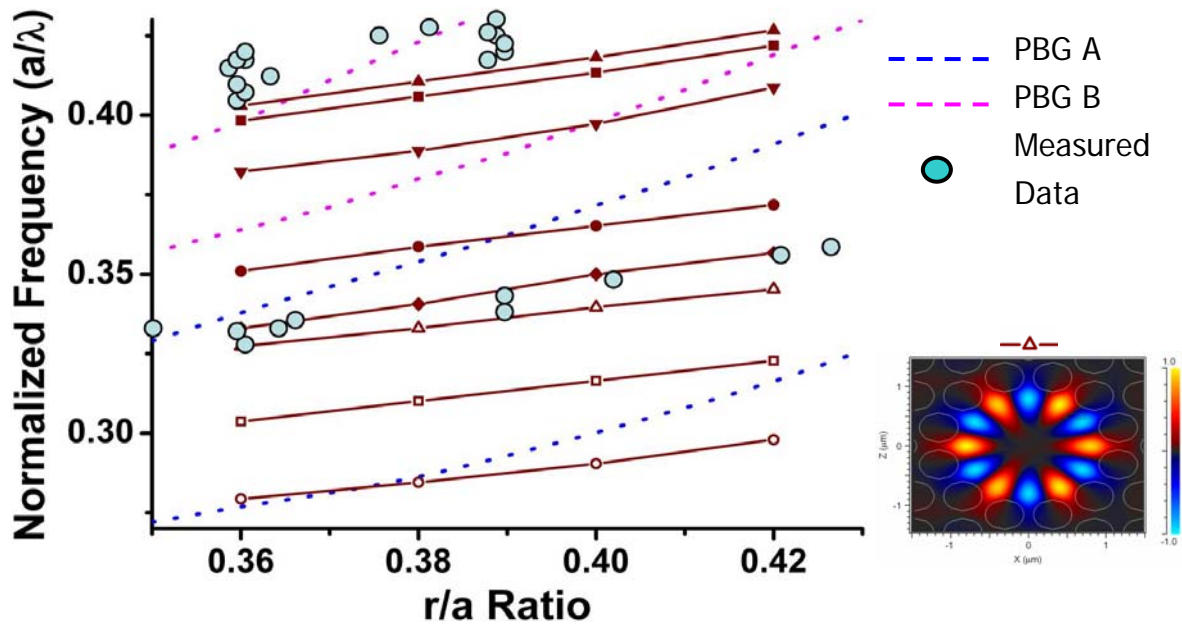


Figure 5.8 The defect modes in normalized frequency of modified 12-fold D2 QPC microcavities. The individual solid circles denote the measured data.

We can also determine the difference of lasing mode between QPC and PC lasers by the characteristic of lasing mode polarization. In the past study, the typical lasing mode of triangular lattice PC is dipole mode. From the measurement results we mentioned above, some of the basic phenomenon for 12-fold QPC and PC lasers is the same, such as mode hopping and lasing wavelength red shifting. But there is a rather different in mode polarization, one characteristic of WGM, was measured in Figure 5.9. The polarized intensity ratio of maximum to minimum for 2-fold QPC and PC lasers is two and 44 times, respectively. Obviously, the peak intensity of QPC lasers was almost the same in any angle and opposite to the triangular lattice PC laser. This result is almost completely conformed to our supposition. Consequently, the data we measured is certainly a kind of WGMs.

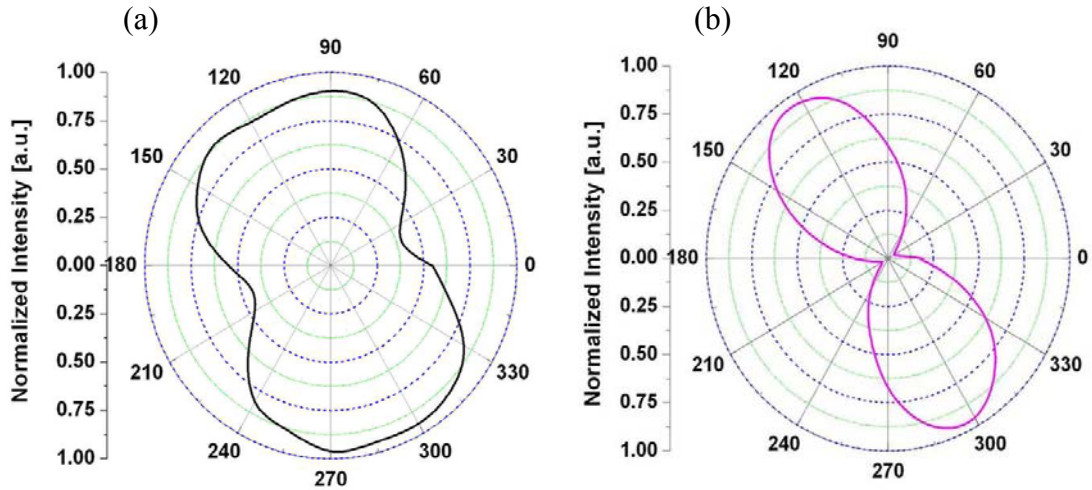


Figure 5.9 Lasing mode polarization of (a) 12-fold QPC lasers (b) triangular lattice PC laser.

We also compare the lasing spectra with and without the central air hole. The modified 12-fold QPC laser was fabricated with a central air hole as shown in Figure 3.13. The measured lasing spectra in dB scale are shown in Figure 5.11. One can see that the side mode is greatly reduced and the SMSR increases from 20 dB to larger than 30 dB after adding a central air-hole. This implies that the modified 12-fold QPC laser is a promising structure for higher Q factor device. And the threshold of the devices without and with central hole is 0.1856 and 0.1504 mW, respectively. The calculated WGM in 12-fold QPC microcavity with and without central air-hole is in Figure 5.10.

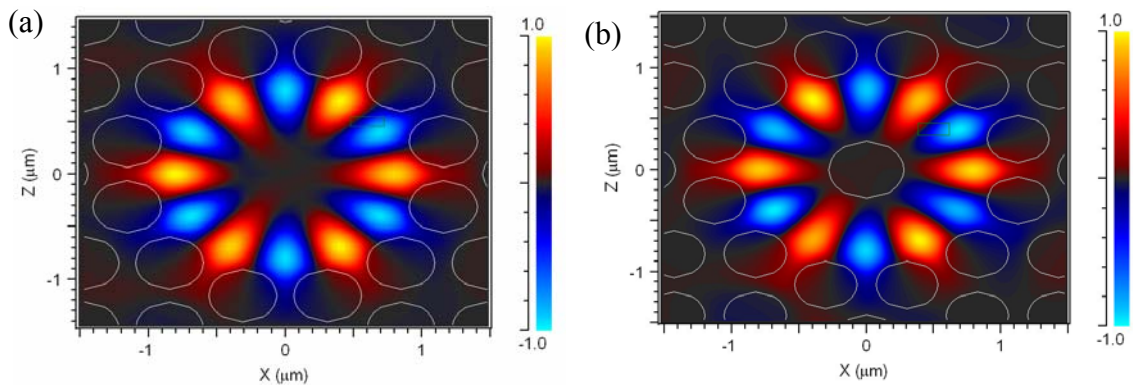


Figure 5.10 (a) The well-confined WGM profile in magnetic field with azimuthal number six of the microcavity without and (b) with a central air-hole.

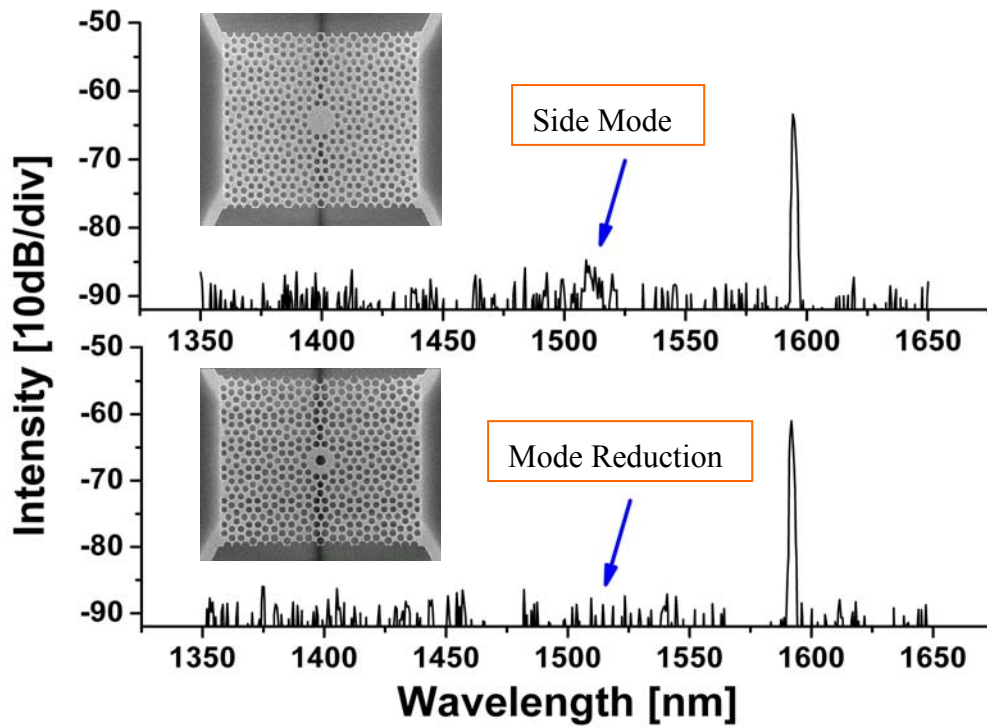


Figure 5.11 The side mode is greatly reduced by inserting the central air hole. The upper and lower lasing spectrum is a 12-fold QPC microcavity without and with a central air hole, respectively.

As we mention in Chapter 2, few groups propose that there are high tolerance in fabrication of QPC lasers. But they have no any confirmation in experiment. Here, we fabricated two different random methods in 24 arrays with different varying lattice constant by design. First, vary the inner-most air-holes (R1) in D2 QPC microcavity laser from 0% to 7% lattice constant position (Fig. 5.12). Second, vary the lattice constant of 2nd, 3rd and 4th layer (R3) in D2 QPC microcavity laser with the same conditions but the inner-most air-holes were fixed on the proper position of lattice constant. Two arrays of the lasing spectra with the random varying lattice constant at the same pumping conditions were shown in Figure 5.13.

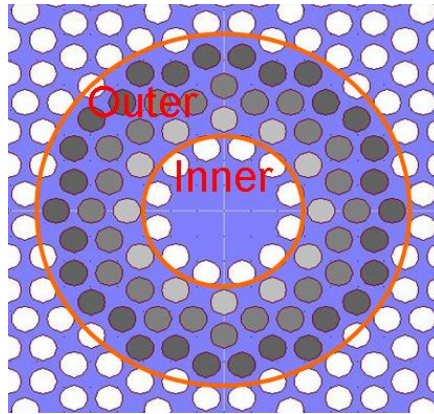


Figure 5.12 The illustration shows the inner-most layer (R1) and the outer layer (R3) air-holes in D2 QPC microcavity laser.

Comparing the schemes in Figure 5.13, we can get two conclusions to the random varying lattice constant PC lasers. In the array of varying lattice constant in the inner-most air hole QPC lasers, the lasing peak wavelength will shift in ± 10 nm disorder scattered (Fig 5.13(a)). In opposite, the array of R3 QPC lasers, the lasing peak wavelength will also shift randomly but concentrate in ± 3 nm. Consequently, the fabrication tolerance to lattice constant varying of R1 is domination to the lasing wavelength shifting. On the other hand, varying the lattice constant of 2nd, 3rd and 4th layer (R3) in D2 QPC microcavity laser will not influence the lasing wavelength shifting seriously. The other conclusion is that the fabrication tolerance is up to 5% lattice constant shifting in R1 and 7% in R3. Therefore, the lasing mode of 12-fold QPC laser is sensitivity to the position of inner-most air-holes. If there is a good controlling in fabrication, the lasing mode will be enhanced more stable. Table 5.1 shows the devices lasing rate with random varying lattice constant in statistic over 300 samples. These results also supply a powerful demonstration to the supposing of high tolerance in QPC lasers. We also measured two columns of thresholds of the random varying lattice constant PC lasers in Table 5.2. Obviously, the thresholds are serious shifting randomly

in R1. The results also proved that the lasing mode of 12-fold QPC laser is sensitivity to the position of inner-most air-holes.

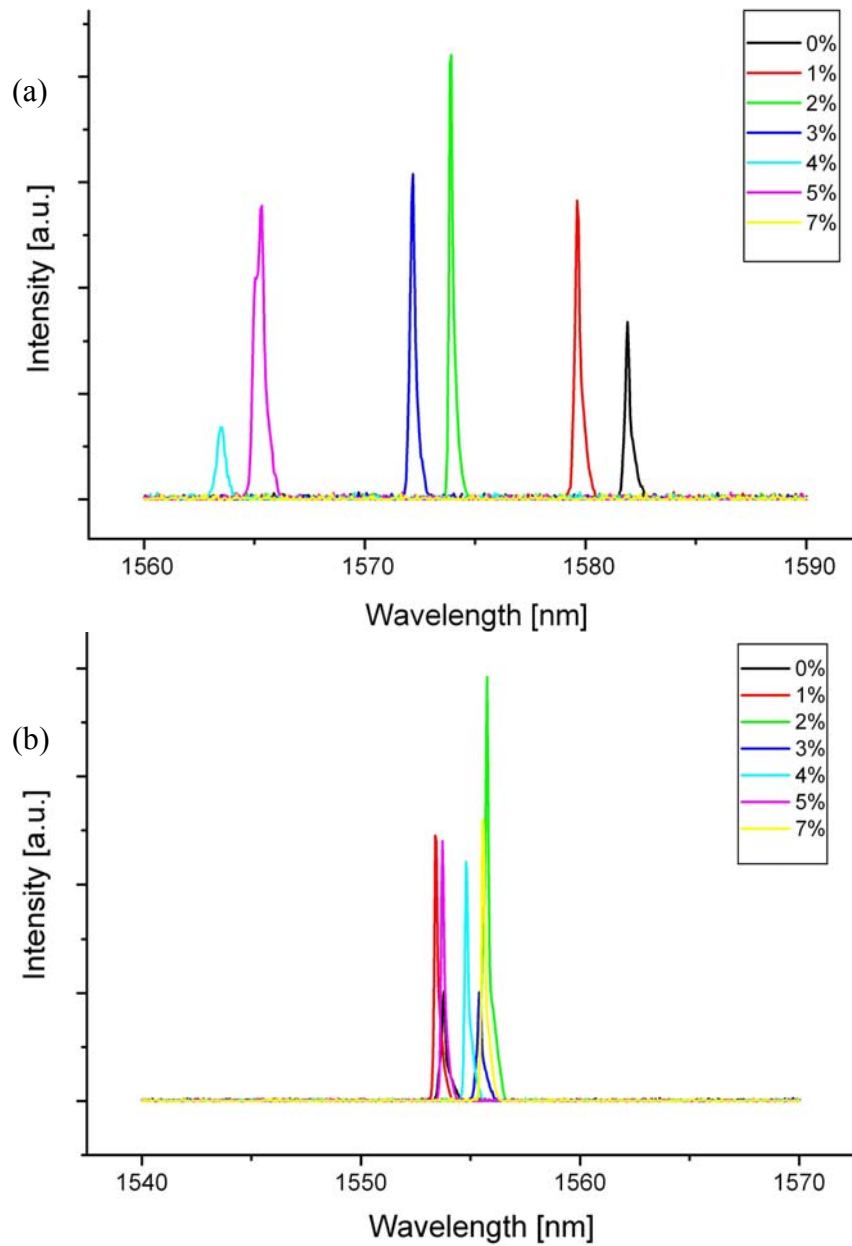


Figure 5.13 The scheme shows the lasing spectrum with the random varying of lattice constant. (a) Vary the inner-most air-holes in D2 QPC microcavity laser from 0% to 7% lattice constant position. (b) Vary the 2nd, 3rd and 4th layer air hole in D2 QPC microcavity laser from 0% to 7% lattice constant position. Nevertheless, the inner-most air-holes were fixed on the proper position of lattice constant.

Table 5.1 Table shows the devices lasing rate with random varying lattice constant in statistic over 300 samples.

Variation	R1	R3
4%	100%	100%
5%	70%	100%
7%	45%	90%

Table 5.2 The table shows the threshold with random varying of lattice constant in 12-fold QPC lasers.

Variation	R1	R3
0%	0.253 mW	0.2464 mW
3%	0.5728 mW	0.24 mW
4%	0.9056 mW	0.2372 mW
5%	0.4 mW	0.2336 mW
7%	No-lasing	0.24 mW

5.2.2. Measurement Results from DBR-Bonding Structures

After the DBR-bonding process, we use the micro-PL system to measure the quality of the bonded wafers. And then we can choose a better enhancement wafer and the smoother surface to do the PC pattern definition process. The lasing spectrum of a typical two-dimensional photonic crystal laser with DBR-bonded wafer at CW pumping condition is shown as following figure. The characteristic of two bonded wafer were measured in Figure 5.13. The numbers in the insert represent the measurement position of a wafer from the center (number 2) to the edge. And the reference is the measurement of the MQWs wafer before DBR substrate bonding. The pulse means change the CW pumping into pulse condition, 0.5 % duty cycle at 0.2MHz repetition rate, in order to check the enhancement is the same doing in pulse pumping condition.

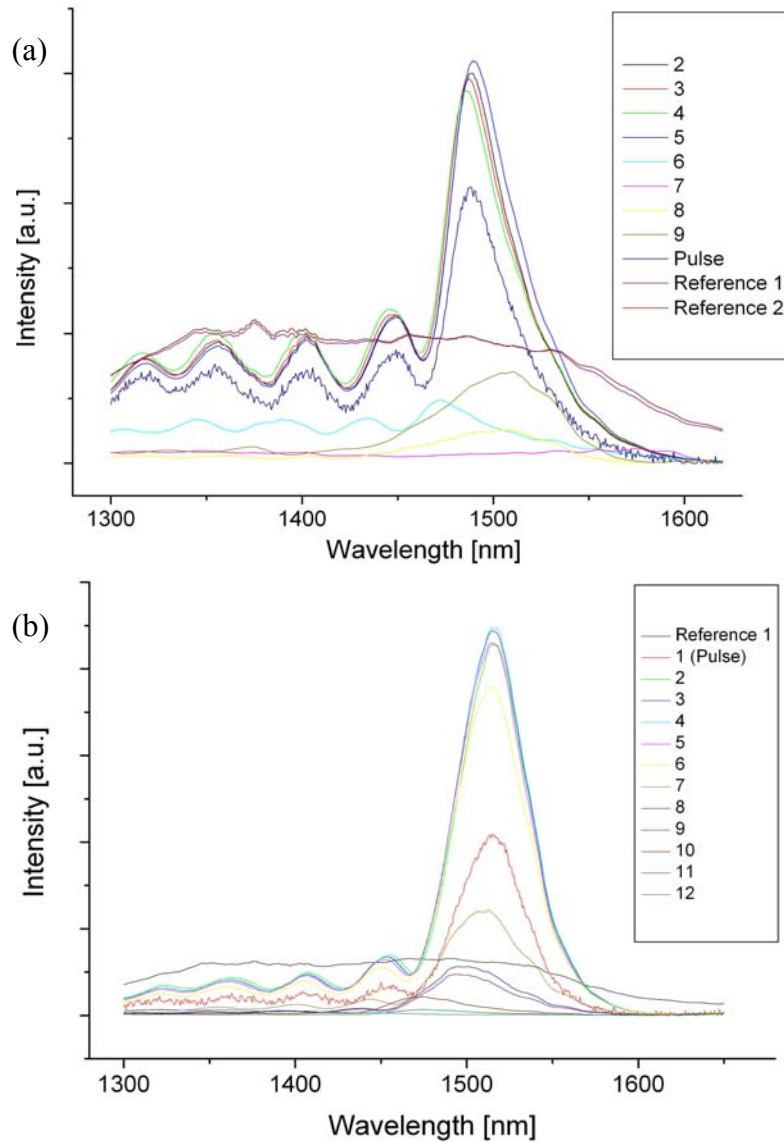


Figure 5.14 The illustrations show the two different DBR-bonded wafer. The numbers represent the measurement position of a wafer from the center (number 2) to the edge.

In Figure 5.14 (a), it illustrated the characteristic of one sample which bonded not very well. The lasing spectrum was shifting in resonance wavelength starting at data 6. It meaning the MQWs was destroyed in wafer bonding process. From the data 7 to 9, the intensities of the lasing spectra were decreased sharply and the Fabry-Perot phenomenon from DBR substrate were also disappear. It implied the important information that the MQWs did not bonded on the DBR substrate. In opposite, the

characteristic of a sample which was bonded better is shown in Figure 5.14 (b). The average length of Fabry-Perot phenomenon is 45nm. From the calculation, we can estimate the location of reflector is about $7\mu\text{m}$ where is at the end of DBR pair. This result is close to the result from simulation. And we can know that the Fabry-Perot phenomenon is caused by the bonded DBR substrate.

The area where is not bonded only occurred at the edge of wafer and the phenomenon of MQWs destroyed appear at the region where is close to the edge. That is a usual phenomenon for fusing two different lattice constant wafers in wafer bonding process. A better bonded sample was determined by its enhancement and a border available area for later processes. In Figure 5.15, we compared the two different bonded wafers that we mentioned above. A better bonded wafer can get the intensity enhancement up to 9 times but the other one is only to 3 times. Furthermore, a good bonded wafer has better smoothness on surface than the other one from the measurement in any points. In conclusion, the wafer fusion process dominates the characteristic of PC Lasers.

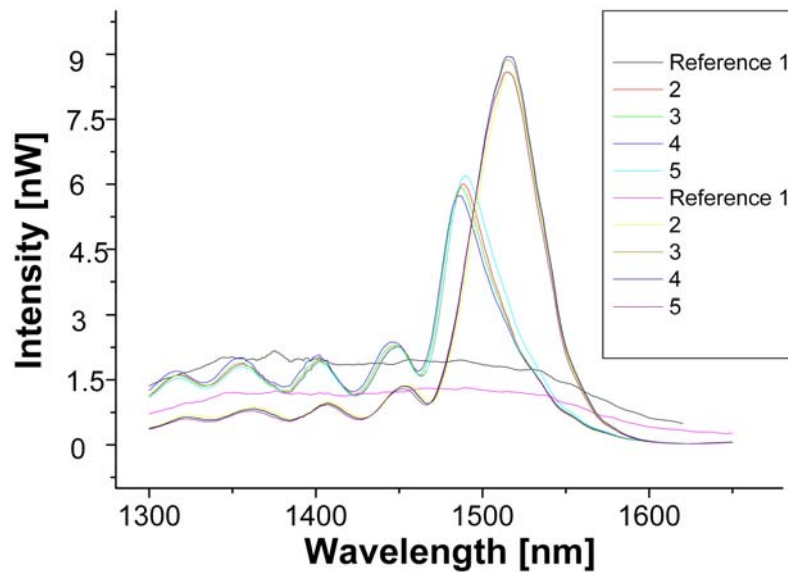


Figure 5.15 The comparison of two different bonded wafer. The enhancement of two wafers is 3 and 9 times, respectively.

After choosing the better bonding region, the PC patterns were defined on the QWs with DBR substrate. The Figure 5.16 shows the lasing mode spectrum of triangular lattice D2 PC lasers. The lasing wavelength is 1498.8 nm and the FWHM is about 0.6 nm. The insert of Figure 5.16 shows the threshold is about 1.76 mW.

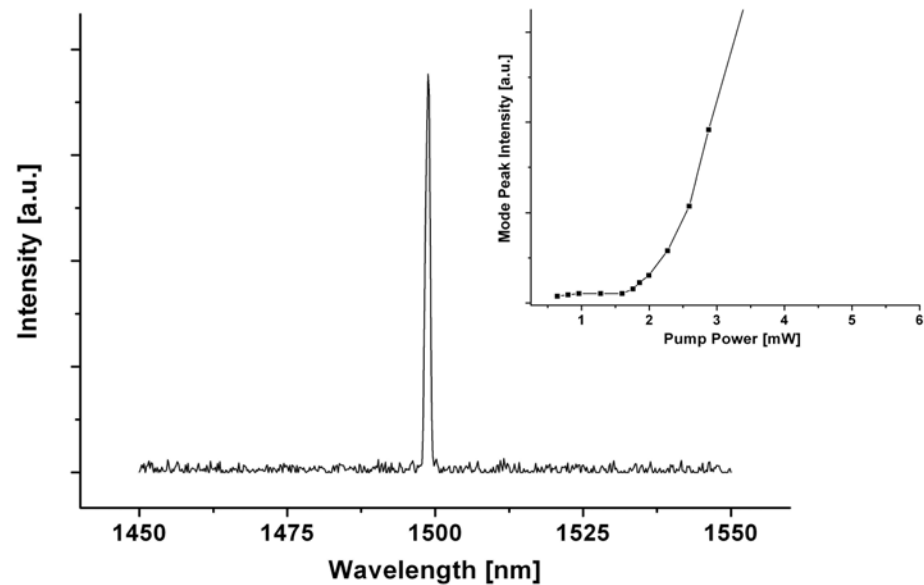


Figure 5.16 The lasing mode spectrum and L-L curve (the insert) of triangular lattice D2 PC lasers with bonded DBR substrate.

The measurement results were not as good as the exception in theory, especially in wider FWHM and higher threshold. We suppose that the bad result is owing to the not enough practiced fabrication or the design of DBR substrate. The better characteristics of PCs on DBR bonded wafers are expected after the improvement in the future.

5.3. Conclusion

In the first section of this chapter, we introduced a NIR micro-PL system with nano-scale spectrum resolution measure all of the devices. In the second section, the basic characteristics of PC/QPC membrane structure lasers and wafer bonding structure lasers were obtained.

At first, the good lasing spectrum was illustrated for a narrow FWHM and high Q factor 12-fold QPC laser. And then, compare the L-L curve between D2, D3 QPC and triangular PC lasers for ultra-small threshold. All of the resonance modes of D2 QPC micro-cavity laser are measured and being fit on the corresponding defect modes in simulation. The mode hopping phenomenon in QPC laser was obtained as the triangular and square PC laser. We recognized the difference lasing mode between QPC and PC laser further by the characteristic of polarization. A modified 12-fold QPC laser was also demonstrated in this chapter. Finally, we use a great quantity of data to suppose that the lasing mode of 12-fold QPC laser is sensitivity to the position of inner-most air-holes.

The last section, these lasing spectra show the quality of the bonded sample. We compare some bonded sample and analyze the characteristic of that. The characteristics of PC lasers with DBR substrate were obtained.

Chapter 6 Conclusion

In my thesis, we introduced the history briefly and the basic theory of photonic crystals in the first chapter. Further, the application of photonic crystals to microcavity lasers and the evolution of that were also being presented.

And then, we calculated the band diagrams, photonic band gaps, resonance spectra, and lasing mode profiles of the symmetric and asymmetric two-dimensional photonic crystal lasers using 3D plane-wave-expansion method and finite-difference time-domain method. These help us to optimize our photonic crystal design. According to these design, we could do a good align between the resonance modes and gain spectrum of MQWs. Furthermore, a modified quasi-periodic photonic crystal microcavity laser was designed.

In the fabrication, we introduced the procedures for two different structures. In the membrane structure, we demonstrated not only the basic photonic crystal lasers but few kinds of the quasi-periodic photonic crystal lasers for different research. And the modified quasi-periodic photonic crystal microcavity lasers were fabricated. In the asymmetric structure, the wafer fusion technology was developed. And the PC microcavity structure was defined on the bonded sample successfully. All of the fabrication procedures for symmetric or asymmetric structure lasers were presented in detail.

In order to characterize the QPC/PC lasers, a micro-scale photoluminescence system was used for measurement. The micro-scale and nano-scale resolutions in microscopic system and spectrum analysis have been achieved. An excellent sensitivity of this system is presented in the chapter of measurement.

By using this system, the basic characteristics of two-dimensional quasi-periodic photonic crystal microcavity were measured. Furthermore, the characteristics were compared to the triangular lattice photonic crystal lasers. The characteristic of modified 12-fold QPC lasers were also demonstrated. And we use a great quantity of data to suppose that the lasing mode of 12-fold QPC laser is sensitivity to the position of inner-most air-holes. The quality of the bonded samples was illustrated by the lasing spectra. We compare some bonded sample and analyze the characteristics of them. And the spectra and the characteristics of PC laser were obtained.



References

- [1] E. Yablonovitch, *Phys. Rev. Lett.*, **vol. 58**, pp. 2059-2062, 1987.
- [2] J. D. Joannopoulos, R. D. Meade, and J. N. Winn, *Princeton University Press*, 1995.
- [3] J. F. Klem, and D. k. Serkland, *J. Vac. Sci Technol. B*, **vol. 22(3)**, pp. 1468-1471, 2004.
- [4] T. D. Happ, A. Markard, M. kamp, A. Forchel, S. Anand, J.-L. Gentner, and N. Bouadma, *J. Vac. Sci Technol. B*, **vol. 19**, pp. 2775-2778, 2001.
- [5] M. Boroditsky, T. F. Karuss, R. Coccioli, R. Vrijen, R. Bhat, and E. Yablonovitch, *Appl. Phys. Lett.*, **vol. 75**, pp.1036-1038, 1999.
- [6] A. J. Danner, J. J. Raftery Jr., N. Yokouchi, and K. D. Choquette, *Appl. Phys. Lett.*, **vol. 84**, pp. 1031-1033, 2004.
- [7] S. Olivier, C. J. M. Smith, H. Benisty, C. Weisbuch, T. F. Krauss, R. Houdre, and U. Oesterle, *IEEE J. Quantum Electron*, **vol. 38(7)**, pp. 814-816, 2002.
- [8] S. Noda, A. Chutinan, and M. Imada, *Nature*, **vol. 407**, pp. 608-610, 2000.
- [9] H.-Y. Ryu, S.-H. Kim, H.-G. Park, J.-K. Hwang, Y.-H. Lee, and J.-S. Kim, *Appl. Phys. Lett.*, **vol. 80**, pp. 3883-3885, 2002.
- [10] K. Hennessy, C. Reese, A. Badolato, C.-F. Wang, A. Imamoglu, G. Jinm, S. Shi, and D.-W. Prather, *Appl. Phys. Lett.*, **vol. 83**, pp. 3650-3652, 2003.
- [11] O. Painter, J. Vuckovic, and A. Scherer, *J. Opt. Soc. Amer. B*, **vol. 16**, pp. 275-285, 1999.
- [12] H.-Y. Ryu, H.-G. Park, and Y.-H. Lee, *IEEE J. Select. Topics Quantum Electron.*, **vol. 4**, pp. 891-908, 2002.
- [13] O. Painter, R.-K. Lee, A. Scherer, A. Yariv, J. D. O'Brien, P. D. Dapkus, and I. Kim, *Science*, **vol. 284**, pp. 1819-1821, 1999.
- [14] Y. Akahane, T. Asano, B.-S. Song, and S. Noda, *Nature (London)*, **vol.425**, pp. 944-947, 2003.

- [15] Y. S. Chan, C. T. Chan, and Z. Y. Liu, *Phys. Rev. Lett.*, **vol. 80(5)**, pp. 956-959, 1998.
- [16] M. E. Zoorob, M. D. B. Charlton, G. J. Parker, J. J. Baumberg, and M. C. Netti, *Nature*, **vol. 404**, pp. 740-743, 2000.
- [17] K. Nozaki, A. Nakagawa, D. Sano, and T. Baba, Member, IEEE, *IEEE J. Select. Topics Quantum Electron.*, **vol. 9(5)**, pp. 1355-1360, 2003.
- [18] S.-K. Kim, J.-H. Lee, S.-H. Kim, I.-K. Hwang, and Y.-H. Lee, *Appl. Phys. Lett.*, **vol. 86(1)**, pp. 1-3, 2005.
- [19] C. Jin, B. Cheng, B. Man, Z. Li, and D. Zhang, *Appl. Phys. Lett.*, **vol. 75(13)**, pp. 1848-1850, 1999.
- [20] C. Jin, B. Cheng, B. Man, Z. Li, and D. Zhang, *Phys. Rev. B*, **vol. 61(16)**, pp. 10762-10767, 2000.
- [21] P.-T. Lee, J. R. Cao, S.-J. Choi, Z.-J. Wei, J. D. O'Brien, and P. D. Dapkus, *Appl. Phys. Lett.*, **vol. 81(18)**, pp. 3311-3313, 2002.



Vita

Feng-Mao Tsai was born at 02, Aug. 1982 in Taipei City, Taiwan.

He received the B.S. degree in engineering and system science from National Tsing Hua University, Hsinchu, Taiwan in 2004. The M.S. degree will receive in department of photonics and display institute from National Chiao Tung University, Hsinchu, Taiwan in 2006.



His research include the design and fabrication of photonic crystal devices III-V semiconductor based photonic crystals and photonic crystal microcavities.

Publications :

- [01] Feng-Mao Tsai, Po-Tsung Lee, Tien-Chang Lu, “Fabrication and Characteristics of Two-dimensional Quasi-period Photonic Crystal Lasers”, *OPT*, A-FR-I 1-1, 2005.
- [02] Po-Tsung Lee, Tsan-Wen Lu, Feng-Mao Tsai, and Tien-Chang Lu, “Lasing Actions of Octagonal Quasi-periodic Photonic Crystal Micro-Cavities”, *IPRM*.
- [03] Po-Tsung Lee, Tsan-Wen Lu, Feng-Mao Tsai, Tien-Chang Lu, and Hao-Chung Kuo, *Appl. Phys. Lett.*, vol. **88(22)**, 201104 (2006).
- [04] Feng-Mao Tsai, Po-Tsung Lee, Tsan-Wen Lu, Tien-Chang Lu, and Hao-Chung Kuo, “Fabrication and Characteristics of Two-Dimensional Quasi-Periodic Photonic Crystal Lasers”, *CLEO*, CMKK6, 2006.
- [05] Tsan-Wen Lu, Feng-Mao Tsai, Po-Tsung Lee, and Tien-Chang Lu, “Modified Octagonal Quasi-Periodic Photonic Crystal Single-Defect Micro-Cavity Lasers”, *CLEO*, JWB11, 2006.